

**FLOW COEFFICIENT PREDICTION OF A BOTTOM LOAD BALL  
VALVE USING COMPUTATIONAL FLUID DYNAMICS**

by

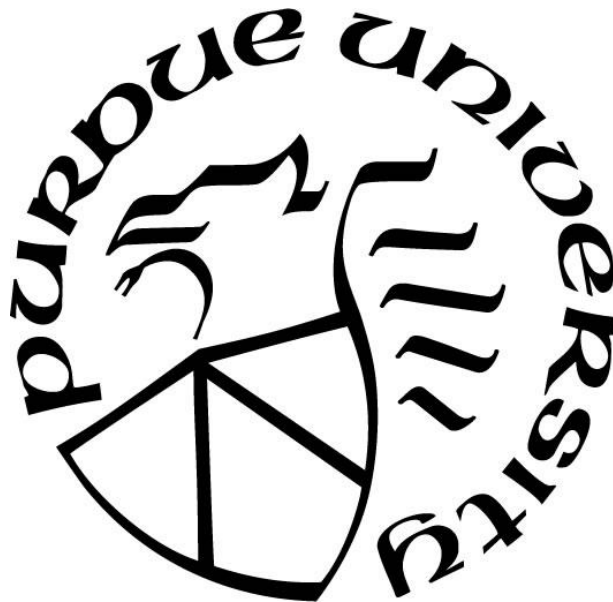
**Daniel A Gutierrez**

**A Thesis**

*Submitted to the Faculty of Purdue University*

*In Partial Fulfillment of the Requirements for the degree of*

**Master of Science**



School of Engineering Technology

West Lafayette, Indiana

May 2019

**THE PURDUE UNIVERSITY GRADUATE SCHOOL  
STATEMENT OF COMMITTEE APPROVAL**

Dr. Mark French, Chair

School of Engineering Technology

Dr. José Garcia Bravo

School of Engineering Technology

Mr. Paul McPherson

School of Engineering Technology

**Approved by:**

Dr. Duane Dunlap

Head of the Graduate Program

*To my mother, Alma, who has always driven me to be the best version of myself that I can be. To my father, Jose, for being the calm, steady hand I always needed.*

## **ACKNOWLEDGMENTS**

Special thanks to Dr. French for always being available to discuss my research and for taking me in as a graduate student.

To Aaron Reid and the engineering department at Banjo Corporation, thank you for all the support, resources, and access to facilities. This study would not have existed without you.

## TABLE OF CONTENTS

LIST OF TABLES .....	8
LIST OF FIGURES .....	9
LIST OF ABBREVIATIONS.....	11
GLOSSARY .....	12
ABSTRACT.....	13
CHAPTER 1. INTRODUCTION .....	14
1.1 Problem Statement .....	14
1.2 Research Question .....	15
1.3 Scope.....	15
1.4 Significance.....	17
1.5 Assumptions.....	19
1.6 Limitations .....	19
1.7 Delimitations.....	20
1.8 Summary.....	20
CHAPTER 2. REVIEW OF LITERATURE .....	21
2.1 Introduction.....	21
2.2 Background Information.....	21
2.3 Previous Studies.....	23
2.3.1 3D CFD Predictions and Experimental Comparisons of Pressure Drop in a Ball Valve at Different Partial Openings in Turbulent Flow .....	23
2.3.2 The Accuracy Degree of CFD Turbulence Models for Butterfly Valve Flow Coefficient Prediction.....	25
2.3.3 Control of Volumetric Flow-Rate of Ball Valve Using V-Port.....	30
2.4 Innovation .....	35
2.5 Summary.....	36
CHAPTER 3. RESEARCH METHODOLOGY.....	37
3.1 Research Framework .....	37
3.2 Testing Methodology .....	37
3.3 Summary.....	38

CHAPTER 4. RESULTS .....	39
4.1 Computational Analysis.....	39
4.1.1 Fluid Domain Creation .....	39
4.1.2 Meshing .....	41
4.1.3 Y+ Boundary Layer .....	46
4.1.4 Boundary Conditions & Simulation Settings .....	47
4.1.5 Fluid Properties.....	48
4.1.6 Turbulence Models .....	49
4.1.7 Result Interpretation .....	50
4.1.7.1 Standard Ball Design .....	50
4.1.7.2 1 <sup>st</sup> Ball Design Iteration .....	53
4.1.7.3 2 <sup>nd</sup> Ball Design Iteration .....	55
4.1.7.4 Comparison of Three Ball Designs .....	58
4.2 Physical Experimentation .....	60
4.2.1 Purpose .....	60
4.2.2 Test Specimen.....	61
4.2.3 Equipment.....	61
4.2.4 Testing Procedure .....	64
4.2.5 Experimental Results.....	65
4.2.5.1 Standard Ball Design .....	65
4.2.5.2 First Ball Design.....	66
4.2.5.3 Second Ball Design .....	67
4.2.5.4 Comparison of Three Ball Designs .....	68
4.2.6 Sources of Error .....	70
4.3 Comparison of Experimental and Computational Results.....	71
4.3.1 Comparison of Flow Coefficient Curves.....	71
4.3.2 Comparison of R <sup>2</sup> Values .....	73
CHAPTER 5. SUMMARY, CONCLUSIONS, and RECOMMENDATIONS.....	76
5.1 Summary.....	76
5.2 Conclusions.....	77
5.3 Recommendations.....	77

LIST OF REFERENCES ..... 78  
APPENDIX..... 80

## LIST OF TABLES

<i>Table 4.1: Skewness and Corresponding Cell Quality</i> .....	42
<i>Table 4.2: Mesh Comparison</i> .....	45
<i>Table 4.3: Comparison of Turbulence Models</i> .....	50
<i>Table 4.4: Computational Analysis of Standard Ball</i> .....	51
<i>Table 4.5: Computational Analysis of 1<sup>st</sup> Ball Design Iteration</i> .....	53
<i>Table 4.6: Computational Analysis of 2<sup>nd</sup> Ball Design Iteration</i> .....	56
<i>Table 4.7: Experimental Test Data (Standard Ball)</i> .....	65
<i>Table 4.8: Experimental Test Data (First Ball Design)</i> .....	66
<i>Table 4.9: Experimental Test Data (2<sup>nd</sup> Ball Design)</i> .....	67

## LIST OF FIGURES

<i>Figure 1.1: Ball Valve Cross Section</i> .....	14
<i>Figure 1.2: Needle Valve Cross-Section</i> .....	15
<i>Figure 1.3: Standard Design (left), Design 1 (center), Design 2 (right)</i> .....	16
<i>Figure 1.4: Bottom-Load Ball Valve</i> .....	16
<i>Figure 1.5: Standard ball (left) vs. V-Slot balls (right)</i> .....	18
<i>Figure 2.1: Effects of Re on <math>C_v</math></i> .....	24
<i>Figure 2.2: Butterfly Valve Cross-Section</i> .....	27
<i>Figure 2.3: Flow Capacity at <math>\theta = 40^\circ</math></i> .....	28
<i>Figure 2.4: Flow Capacity at <math>\theta = 60^\circ</math></i> .....	29
<i>Figure 2.5: Flow Capacity at <math>\theta = 70^\circ</math></i> .....	29
<i>Figure 2.6: Various V-Port Designs</i> .....	30
<i>Figure 2.7: Flow Coefficient of <math>90^\circ</math> V-Port</i> .....	32
<i>Figure 2.8: Flow Coefficient of <math>60^\circ</math> V-Port</i> .....	32
<i>Figure 2.9: Flow Coefficient of <math>30^\circ</math> V-Port</i> .....	33
<i>Figure 2.10: Effects of V-Ports on Flow Coefficient</i> .....	34
<i>Figure 2.11: Effect of V-Ports on Cavitation Index</i> .....	35
<i>Figure 4.1: Half-Section of Bottom-Load Ball Valve</i> .....	40
<i>Figure 4.2: 3D model of Fluid Domain for Standard Ball Design</i> .....	41
<i>Figure 4.3: Mesh of Standard Ball at Fully Open Position</i> .....	42
<i>Figure 4.4: Skewness Metrics for Standard Ball Mesh (Coarse)</i> .....	43
<i>Figure 4.5: Fine Mesh of Standard Ball at Fully Open Position</i> .....	44
<i>Figure 4.6: Skewness Metrics for Standard Ball Mesh (Fine)</i> .....	45
<i>Figure 4.7: Inflation Layer at Mesh Outlet</i> .....	47
<i>Figure 4.8: Flow-Coefficient vs. Degree of Opening (Standard Ball)</i> .....	51
<i>Figure 4.9: Volumetric Flow-Rate vs. Degree of Opening (Standard Ball)</i> .....	52
<i>Figure 4.10: Cavitation Index vs. Degree of Opening (Standard Ball)</i> .....	53
<i>Figure 4.11: Flow Coefficient vs. Degree of Opening (1<sup>st</sup> Ball Design)</i> .....	54
<i>Figure 4.12: Volumetric Flow-Rate vs. Degree of Opening (1<sup>st</sup> Ball Design)</i> .....	54

<i>Figure 4.13: Cavitation Index vs. Degree of Opening (1<sup>st</sup> Ball Design)</i> .....	55
<i>Figure 4.14: Flow Coefficient vs. Degree of Opening (2<sup>nd</sup> Ball Design)</i> .....	56
<i>Figure 4.15: Flow-Rate vs. Degree of Opening (2<sup>nd</sup> Ball Design)</i> .....	57
<i>Figure 4.16: Cavitation Index vs. Degree of Opening (2<sup>nd</sup> Ball Design)</i> .....	58
<i>Figure 4.17: Comparison of Computational Flow Coefficient Curves</i> .....	59
<i>Figure 4.18: Computational R<sup>2</sup> Comparison of Three Ball Designs (Flow Coefficient)</i> .....	59
<i>Figure 4.19: Computational R<sup>2</sup> Comparison of Three Ball Designs (Flow-Rate)</i> .....	60
<i>Figure 4.20: Test Circuit Schematic</i> .....	61
<i>Figure 4.21: Physical Test Circuit</i> .....	62
<i>Figure 4.22: Omega Pressure Transducer</i> .....	63
<i>Figure 4.23: Magnetic Flowmeter</i> .....	63
<i>Figure 4.24: Angle Indicator</i> .....	64
<i>Figure 4.25: Experimental Flow Coefficient vs. Degree of Opening (Standard Ball)</i> .....	66
<i>Figure 4.26: Experimental Flow Coefficient vs. Degree of Opening (1<sup>st</sup> Ball Design)</i> .....	67
<i>Figure 4.27: Experimental Flow Coefficient vs Degree of Opening (2<sup>nd</sup> Ball Design)</i> .....	68
<i>Figure 4.28: Comparison of Experimental Flow Coefficient Curves</i> .....	69
<i>Figure 4.29: Experimental R<sup>2</sup> Comparison of Three Designs (Flow Coefficient)</i> .....	69
<i>Figure 4.30: Comparison of Flow Coefficient Curves (Standard Ball)</i> .....	71
<i>Figure 4.31: Comparison of Flow Coefficient Curves (1<sup>st</sup> Ball Design)</i> .....	72
<i>Figure 4.32: Comparison of Flow Coefficient Curves (2<sup>nd</sup> Ball Design)</i> .....	72
<i>Figure 4.33: R<sup>2</sup> Comparison of Computational and Experimental Methods</i> .....	73
<i>Figure 4.34: Flow Streamlines of 2<sup>nd</sup> Ball Design</i> .....	74
<i>Figure 4.35: Turbulent Kinetic Energy (2<sup>nd</sup> Ball Design)</i> .....	75
<i>Figure 4.36: Turbulent Kinetic Energy (1<sup>st</sup> Ball Design)</i> .....	75
<i>Figure 0.1: Pressure Transducer Specifications</i> .....	80
<i>Figure 0.2: Magnetic Flowmeter Specifications</i> .....	81

## LIST OF ABBREVIATIONS

CFD – Computational Fluid Dynamic

FEA – Finite Element Analysis

PSI – pounds per square inch,  $\frac{lb}{in^2}$

3D – Three dimensional

CAD – Computer Aided Design

GPM – U.S. Gallons per minute

CAE- Computer Aided Engineering

## GLOSSARY

Actuator – electronic mechanism which controls the opening and closing of a valve.

Bottom-load Ball Valve – a valve in which fluid is redirected 90° from the inlet to outlet.

Boundary Conditions – input parameters for a computational model.

Cavitation Index - is commonly used in industry to describe the possibility of cavitation occurring.

Coefficient of Determination,  $R^2$  - a statistical measure of how close data points are to the fitted regression line.

Flow Coefficient - a dimensionless value that describes the relationship between volumetric flow rate and pressure drop across a device.

Fluid Domain – The empty volume in which fluid can occupy.

Hysteresis - the phenomenon in which the value of a physical property lags behind changes in the effect causing it.

Isotropic – Properties are the same in different directions.

Reynold's Number - a dimensionless value that measures the ratio of inertial forces to viscous forces and describes the degree of laminar or turbulent flow.

## ABSTRACT

Author: Gutierrez, Daniel, A. MS

Institution: Purdue University

Degree Received: May 2019

Title: Flow Coefficient Prediction of a Bottom Load Ball Valve Using Computational Fluid Dynamics

Committee Chair: Mark French

Throughout the fluid handling industry there are several tools used to regulate the distribution of fluids for a given process. The valve, in its many variations, is a commonly used tool found in a variety of processes that regulates flow. Like all products, certain variations of the valve are better suited to specific applications than others.

Just as there are a variety of valves that have benefits and limitations, there are a variety of techniques used to evaluate the effectiveness and performance of valves. Perhaps the most common technique used to evaluate a valve's performance involves computational fluid dynamic (CFD) software. Computational fluid dynamic software provides a numerical approximation of the Navier-Stokes equations, which describe the motion and behavior of viscous fluids and are based on applying Newton's second law of motion to fluid motion (A. Del Toro, 2012). CFD software also provides a numerical approximation to various turbulence models. These turbulence models are often semi-empirical and describe the effects turbulence in fluid flow.

This study analyzed the capability of a CFD model to predict several performance characteristics. The primary characteristic of this study was the flow coefficient. To measure the accuracy of CFD model, its computational results were compared to experimentally gathered data. The results of this study showed that a CFD model can predict flow coefficient to a reasonable degree of accuracy when flow is generally uninterrupted and laminar. However, as the flow grows increasingly turbulent, a CFD model predicts flow coefficient at a decreasing level of accuracy. This study also analyzed several designs and quantified each design's ability to linearly increase flow rate using both a CFD model and experimental data. The results of this study are outlined in the following chapters.

## CHAPTER 1. INTRODUCTION

### 1.1 Problem Statement

In automated processes where the quick and accurate distribution of fluid is desired, a valve which can linearly increase volumetric flow rate as a function of its position provides greater control over the quantity of fluid delivered. Most valves on the market today, specifically ball valves, increase volumetric flow rate non-linearly from the fully closed position to the fully opened position. Ball valves are optimal devices in automated fluid handling because ball valves can rotate from fully closed to fully opened within a full rotation (typically 90°) opposed to the multiple 360° rotations a needle valve or throttle valve must undergo to reach their respective fully open positions.

Although ball valves provide quick and simple actuation, ball valves typically do not have a linear relationship between volumetric flow-rate and valve position. There exists a need in industry for a valve that combines the quick actuation of a ball valve with the capability to increase flow-rate linearly as found in needle valves. Cross-sectional views of both a standard ball valve and needle valve can be seen in figures 1.1 – 1.2.

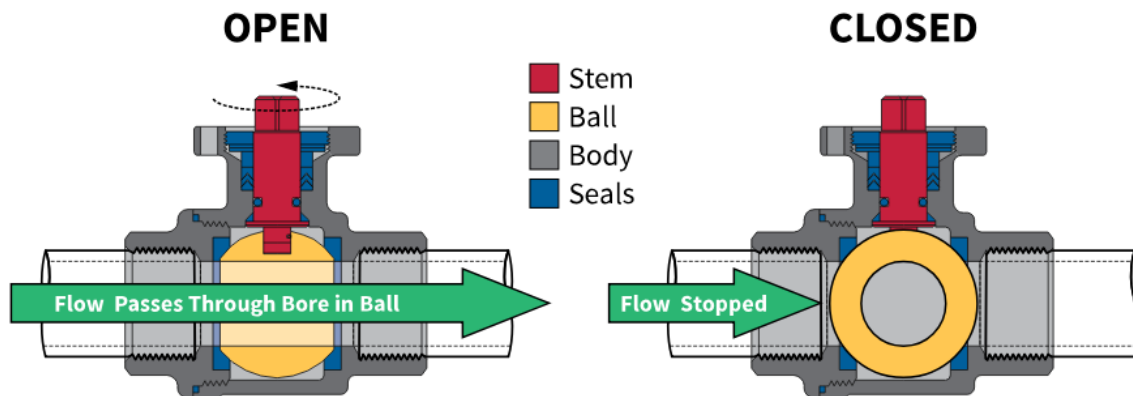


*Figure 1.1:* Ball Valve Cross Section

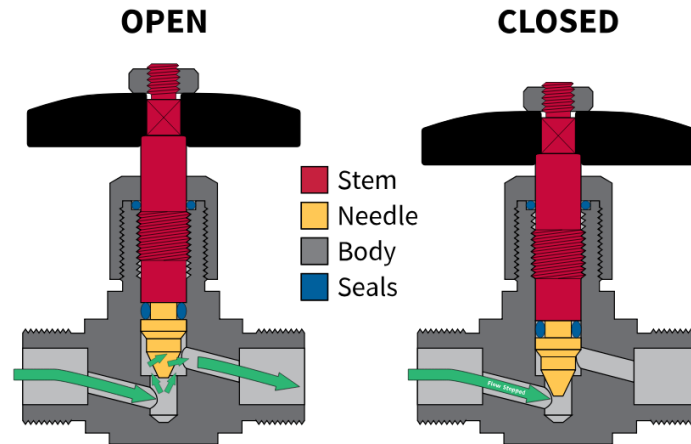


Figure 1.2: Needle Valve Cross-Section

Several design modifications to the ball valve have been analyzed and manufactured to achieve this linear relationship. However, the production of prototype parts and the subsequent experimentation to validate performance can be costly and time-consuming. Developing an accurate and reliable CFD model to analyze ball valve designs would be beneficial.

## 1.2 Research Question

To what degree of accuracy can CFD analysis predict a ball valve design's ability to regulate fluid flow linearly? How can the results from a CFD analysis streamline the design process?

## 1.3 Scope

This study utilized computational methods to predict the flow coefficient of three ball valve designs at various positions in between each design's respective fully closed and fully opened positions. The three ball valve designs in this study are bottom-load valves. Unlike standard ball valves, which direct fluid along a single axis, bottom-load valves direct fluid through a 90° turn. Of the three designs, one is a standard bottom-load ball with three holes that meet at the center of the ball. The other two designs feature an outside groove that gradually increases as the ball is rotated from its fully closed to fully opened positions. Images of each design can be seen in figure 1.3.



*Figure 1.3: Standard Design (left), Design 1 (center), Design 2 (right)*

The standard ball design can rotate from its fully closed to fully opened positions in a  $90^\circ$  turn while designs 1 – 2 must travel approximately  $180^\circ$  to travel from fully closed to fully opened.

The inlet of a bottom load valve is found on the bottom side of the valve and the outlet(s) can be found on any side of the valve that is perpendicular to the axis of the inlet. An image of the bottom-load ball housing that was used for each design in this study can be seen in figure 1.4.



*Figure 1.4: Bottom-Load Ball Valve*

Flow coefficient is a dimensionless value that describes the relationship between volumetric flow rate and pressure drop across a device. The formulation of flow coefficient for incompressible fluids can be seen below in equation (1).

$$C_v = Q \sqrt{\frac{SG}{\Delta P}} \quad (1)$$

Where:

- $C_v$  is the flow coefficient
- $Q$  is the volumetric rate of flow
- $SG$  is the specific gravity of the fluid
- $\Delta P$  is the pressure drop across the valve

In U.S. customary units, flow coefficient is defined as the volume of water (in U.S. gallons) at 60°F that will flow through a valve with a 1 PSI pressure drop across the valve. Holding pressure drop and specific gravity constant, a linear increase in volumetric flow rate produces a linear increase in flow coefficient. A valve with a linear relationship between flow coefficient and ball position will therefore have a linear relationship between volumetric flow rate and ball position.

Several computational methods were evaluated and applied to three ball valve designs. Computational fluid dynamic software was used to simulate fluid flow and predict flow coefficient through each design iteration. Experimental data was collected from 3D printed prototypes to validate any simulations and analyses performed during this study. The experimental data collected was used to compare the accuracy of various computational methods and turbulence models.

#### 1.4 Significance

Ball valves are desirable for the little motion required to travel from the fully closed to fully open position. Ball valves are also generally more economic alternatives to other valve styles commercially available. The combined benefits of affordability and simple actuation make ball valves an attractive option in the automation of any fluid handling process.

However, the benefits a ball valve can provide are not without limitations. One primary limitation of balls valves is the ability to accurately control flow. The control of flow, in the intermediate positions between fully closed and fully opened, is difficult to achieve. In automated processes, this tends to create cycles of hysteresis where the flow regulating element in a ball valve is rotated in an oscillating manner until the desired flow is obtained. The nonlinear relationship between flow and valve position is a problem many in industry have attempted to solve.

Most attempts to linearize the relationship between valve position and flow rate have focused on changing the flow regulating element in a ball valve; the rotating ball. Traditionally the ball in a ball valve is created with a through hole, which is centered on the axis perpendicular to the axis of rotation. These attempts have changed the geometry of the through hole to what is commonly referred to as a “V” shaped slot. These changes to a ball’s geometry have affected the relationship between flow rate and ball position by various amounts. A comparison of a standard ball and several v-slot balls can be seen in figure 1.5.



*Figure 1.5: Standard ball (left) vs. V-Slot balls (right)*

An in-depth examination of the effects these modifications have on the relationship between flow rate and ball position can be found in Chapter two. Although various valve manufacturers have produced modified standard (in-line) ball valves with improved flow control, manufacturers and academics have yet to thoroughly examine various modifications to bottom-load ball valves that could also improve the ability to regulate flow. The turbulence created by

the 90° turn fluid makes in a bottom-load ball valves makes a computational analysis more complex. Producing a computational model that can accurately predict valve behavior, as has been done in standard ball valves, would be beneficial.

### 1.5 Assumptions

In this study key assumptions made pertain to the nature of the fluid in both the computational analyses and physical experimentation in this study. The assumption of the fluid's material properties was one impactful assumption made during this study. It affected the boundary conditions, governing equations, and simulation results of the computational fluid dynamic simulation. The fluid used in this study was water. The key assumption that was made is that water is a perfect Newtonian fluid, incompressible, and isotropic. A Newtonian fluid is any fluid in which the viscous stress that is developed is linearly proportional to the strain in the same location (Hoffman & Johnson, 2007). Assuming water behaves as a Newtonian fluid reduced the complexity of the governing equations that a CFD algorithm solves. Assuming that water is an incompressible and isotropic fluid also simplified the governing equations a CFD algorithm solves. Making these assumptions leads to a quicker solution time for any CFD software. Although no real fluid perfectly fits the definition of a Newtonian fluid, water can be assumed to be Newtonian for common applications where stress, pressure, and velocity are relatively small (Durran, 1989).

Another key assumption is that the water remained at a constant 60°F during all testing and CFD simulations. If one assumes that temperature of water remains constant at 60°F than the specific gravity of water remains one. This assumption simplified the flow coefficient equation.

### 1.6 Limitations

One limitation to this study is the readily available computational capabilities of the computers available on campus. As in finite element analysis, the number of individual elements in a simulation is one of the primary factors that control a simulation's run time. It is not uncommon for complex simulations to have run times of several hours. To mitigate this constraint, certain delimitations and assumptions have been made to simplify the governing equations that are required to be solved.

Another limitation that affected both the computational and experimental measurement of flow coefficient was the ability to manufacture each ball design with the same material. Standard ball designs were readily available in 316 stainless steel, however, designs 1 – 2 had to be 3D printed out of ABS plastic. Although the designs had different surface roughness values, each design was modeled to have same surface roughness in its respective computational analysis. The discrepancy between modeled surface roughness and actual surface roughness is one limitation that could affect both the measurement and simulation of flow coefficient.

The major limitation affecting the experimental portion of this study was the accuracy of measurement devices used. Unlike measurements from computational methods, pressure was only measured at one point in space and time. A more detailed assessment of each measurement device's accuracy and potential sources of error can be found in chapter four. A more detailed overview of the experimental setup and procedure can also be found in chapter four.

### 1.7 Delimitations

The different angles of opening in a valve that were evaluated in both the computational fluid dynamic simulation and physical experimentation is one prominent delimitation in this study. For the evaluation of the standard ball design a 3D CAD model was created for six unique positions. These unique positions were 15°, 30°, 45°, 60°, 75°, and 90° (fully open). Each angle required a unique 3D model and mesh to run the computational fluid dynamic simulation. This delimitation is set to reduce the long time associated with solving complex computational fluid dynamic problems. Six unique 3D CAD models were also made to evaluate the two other ball designs. Unlike the standard ball design, these designs were evaluated at 30°, 60°, 90°, 120°, 180° (fully open).

The other delimitation in this study was the performance characteristics that were evaluated. There are several performance characteristics commonly used to evaluate a valve, but for the scope of this study only the valve's flow coefficient was evaluated.

### 1.8 Summary

This section covered the research question to be studied and reasoning for it. This section also defined terms used and covered associated assumptions and limits.

## CHAPTER 2. REVIEW OF LITERATURE

This chapter presents an overview of literature topics related to this study.

### 2.1 Introduction

Because this study examines the performance characteristics of a ball valve, with the desired capability of increasing flow-rate linearly, it is appropriate to analyze previous studies of a similar nature. This chapter provides a summary of recent research literature in related topics as well as any gaps in research.

### 2.2 Background Information

When evaluating a valve, understanding the performance characteristics desired is essential to an effective and meaningful analysis. Common performance characteristics include the pressure drop across a valve or fitting, the flow coefficient, Reynold's number, and cavitation index. There are various other characteristics that are often the subject of a study or analysis such as turbulence caused by a valve or volumetric flow rate as a function of valve position.

Traditionally, physical experiments have been conducted to quantify these characteristics. However, the use of computational fluid dynamic software has become a popular and more economical alternative to the fabrication of physical prototypes to conduct tests. Understanding the mathematics behind computational fluid dynamics as well as the factors that affect accuracy is the first step that must be taken when developing a reliable simulation. Computational fluid dynamics or CFD works in a similar manner to finite element analysis. In both computational techniques a volume or part is broken into a finite number of elements of known dimensions. A numerical approximation to a governing equation is then solved throughout each individual element. This numerical approximation works by converting a continuous function into a discrete function. In a finite element analysis, as the size of an element approaches zero, the numerical approximation approaches the theoretical value. Numerical approximations are often used because of the complexity of real-world problems that make solving a continuous function impractical. The continuous functions that describe many physical phenomena, like the Navier-

Stokes equations, are often partial differential equations that are very complex and difficult to solve analytically.

The governing equation, which describes the motion and behavior of all fluids, is typically some variation of the Navier-Stokes equation. For the purpose of evaluating valves, these equations can often be simplified to remove terms that account for physical phenomenon that occur in supersonic flows (Versteeg & Malaskechera, 2007). Once these terms are removed, the Navier-Stokes equations can be re-written to yield simplified equations.

Although most CFD software provides a numerical approximation of the Navier-Stokes equations, the discretization method varies from software to software and is typically dependent on the application and types of flow present; e.g. subsonic or supersonic flows. Discretization refers to the method in which software breaks a part or volume into smaller, discrete elements of known dimensions. In fluid dynamics, the Finite Volume Method (FVM) is often used as the discretization technique. This method is often preferred over others due to its advantages in memory usage and solution speed, particularly for complex simulations and high Reynolds number (turbulent) flows (E. F. Toro, 2009).

As in Finite Element Analysis (FEA), there are other factors that a user controls which can affect the accuracy of a CFD simulation. These factors are often referred to as boundary conditions. Boundary conditions can be described as the chosen parameters of a simulation (Hutton, 2004). In an FEA simulation, which typically deals with structural mechanics, an example of a typical boundary condition is setting the deflection of a structure equal to zero at the location where that structure is supported or fixed. In Finite Element Analysis, this is known as a fixed constraint. The accuracy and reliability of an FEA simulation is dependent on the user correctly choosing and applying these boundary conditions to a simulation. Similarly, there are boundary conditions in computational fluid dynamics which are essential to an accurate simulation. These boundary conditions are often the mass flow rate at the inlet, the velocity of fluid, or the pressure experienced by the fluid. There are several other boundary conditions that a simulation may be subjected to depending on the nature of the problem (Said, AbdelMeguid, & Rabie, 2016).

## 2.3 Previous Studies

### 2.3.1 3D CFD Predictions and Experimental Comparisons of Pressure Drop in a Ball Valve at Different Partial Openings in Turbulent Flow

Although a computational fluid dynamic simulation can be accurate and provide valuable insight to developing a new fluid-handling product, its accuracy must ultimately be verified with experimental data. The comparisons of CFD predictions and experimental data have been the subject of various studies. An article in the *Journal of Energy Engineering* examines the results of a CFD simulation on a fully-flanged ball valve and compares the results to experimental data, for the same valve, that was produced by the American Society of Heating, Refrigerating, and Air-Conditioning Engineers (ASHRAE). The performance characteristic that was the focus of this study was the pressure drop in the ball valve at different partial openings in the presence of turbulent flow (Moujaes & Jagan, 2008).

The study conducted by Moujaes & Jagan also examined other characteristics of a valve that are essential for describing its flow properties. These characteristics are the loss coefficient,  $K$ , and the flow coefficient,  $C_v$ . To validate the accuracy and reliability of their computational fluid dynamic model, Moujaes & Jagan compared the simulation results, of the three previously mentioned parameters, to previously compiled experimental data. Like most CFD models, the governing equation solved in this study was the Navier-Stokes equation. Furthermore, this study also considers the effects of turbulence. To model turbulence, the standard k- $\epsilon$  turbulence model was used. The CFD software used in this study was STAR-CD.

This study ran multiple simulations with varying Reynold's numbers to study its effects on both flow and loss coefficients. The CFD results of this study found that generally the loss and flow coefficients of a valve are independent of the Reynold's number, but tend to change as a valve travels from its closed to open positions. Figure 2.1 illustrates the effect that Reynold's number has on the flow coefficient of a ball valve.

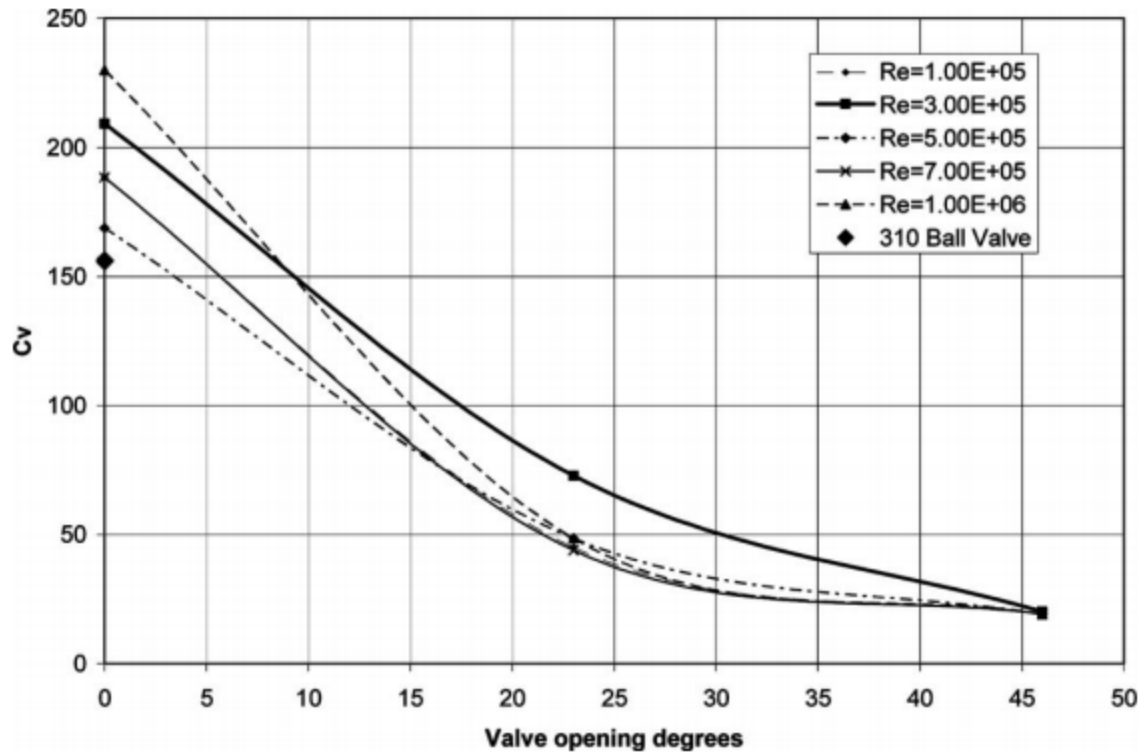


Figure 2.1: Effects of Re on  $C_v$

CFD simulations of the ball valve in this study show that as the ball rotates from its fully closed position to its fully opened position the loss coefficient tends to decrease. The flow coefficient tends to increase as the ball rotates from fully closed to fully opened. In the figure 2.1,  $0^\circ$  is referred to as fully open. The conclusion of this study was that the results of the CFD simulation agree reasonably well with recently published experimental results. The experimental and computational results show that flow coefficient and loss coefficient are independent of Reynold's number (Moujaes & Jagan, 2008). This conclusion can streamline future studies by eliminating the need to run multiple computational simulations with varying Reynold's numbers.

Although the study produced by Moujaes & Jagan demonstrated that a computational fluid dynamic model can be used to determine performance characteristics to a reasonable degree of accuracy and reliability, there are some limitations not mentioned by either author. The primary limitation of this study is that only one turbulence model was utilized. In the field of computational fluid dynamics, there are several turbulence models with varying degrees of

complexity. Each turbulence model provides a unique set of advantages and disadvantages, with no one turbulence model accepted as the industry standard.

### 2.3.2 The Accuracy Degree of CFD Turbulence Models for Butterfly Valve Flow Coefficient Prediction

A study published by Dr. Said, Dr. AbdelMeguid, and Dr. Rabie examined the accuracy of multiple turbulence models for the prediction of the flow coefficient of a butterfly valve. Other than examining the performance characteristics of a different type of valve, this study also differs from the previous in that its authors compare the accuracy of multiple turbulence models where the study by Moujaes & Jagan only considers a single turbulence model. This study examines the accuracy of the standard k- $\varepsilon$  turbulence model, the realized k- $\varepsilon$  turbulence model, the k- $\omega$  model, and the Reynold's stress equation model. By examining the differences between models, the authors of this study can draw conclusions as to the accuracy of a model in the presence of certain boundary conditions, mesh density, element quality, and several other parameters. The study by Moujaes & Jagan failed to consider the differences produced by varying turbulence models.

The standard k- $\varepsilon$  turbulence model is a semi-empirical two-equation model that describes the behavior of fluids in turbulent flow. The two equations are partial differential equations that define the turbulent kinetic energy and the rate of dissipation of turbulence energy (Hoffman & Johnson, 2007). The equations for turbulent kinetic energy,  $k$  and dissipation,  $\varepsilon$  are shown below in equations (2) – (3):

$$\frac{\partial(\rho k)}{\partial t} + \frac{\partial(\rho k u_i)}{\partial x_i} = \frac{\partial}{\partial x_j} \left[ \frac{\mu_t}{\sigma_k} \frac{\partial k}{\partial x_j} \right] + 2\mu_t E_{ij} E_{ij} - \rho \varepsilon \quad (2)$$

$$\frac{\partial(\rho \varepsilon)}{\partial t} + \frac{\partial(\rho \varepsilon u_i)}{\partial x_i} = \frac{\partial}{\partial x_j} \left[ \frac{\mu_t}{\sigma_\varepsilon} \frac{\partial \varepsilon}{\partial x_j} \right] + C_{1\varepsilon} \frac{\varepsilon}{k} 2\mu_t E_{ij} E_{ij} - C_{2\varepsilon} \rho \frac{\varepsilon^2}{k} \quad (3)$$

Where:

- $\mu_i$  is the velocity component in the corresponding direction
- $E_{ij}$  is the component of rate of deformation

- $\mu_t$  is the eddy viscosity

Because the standard k- $\varepsilon$  model is semi-empirical, there are several constants that have been derived by several iterations of data fitting throughout time. These constants are  $\sigma_k$ ,  $\sigma_\varepsilon$ ,  $C_{1\varepsilon}$ , and  $C_{2\varepsilon}$ . As the most commonly used turbulence model in computational fluid dynamics, it is appropriate to thoroughly describe the standard k- $\varepsilon$  model and the terms that define its formulation.

The realized k- $\varepsilon$  turbulence model is very similar to the standard model, but differs in that the formulation for eddy viscosity, which describes the large-scale transport and dissipation of shear energy in a fluid, is a variable rather than a constant (Said et al., 2016). The realized k- $\varepsilon$  turbulence model also differs from the standard model in that the partial differential equation that defines the rate of dissipation of turbulent energy is derived from a different equation. The equations for the realizable k- $\varepsilon$  model can be seen below in equations (4) – (5).

$$\frac{\partial}{\partial t}(\rho k) + \frac{\partial}{\partial x_j}(\rho k u_j) = \frac{\partial}{\partial x_j} \left[ \left( \mu + \frac{\mu_t}{\sigma_k} \right) \frac{\partial k}{\partial x_j} \right] + G_k + G_b - \rho \varepsilon - Y_M + S_k \quad (4)$$

$$\frac{\partial}{\partial t}(\rho \varepsilon) + \frac{\partial}{\partial x_j}(\rho k \varepsilon) = \frac{\partial}{\partial x_j} \left[ \left( \mu + \frac{\mu_t}{\sigma_\varepsilon} \right) \frac{\partial \varepsilon}{\partial x_j} \right] + \rho C_{1\varepsilon} S_\varepsilon - \rho C_{2\varepsilon} \frac{\varepsilon^2}{k + \sqrt{\nu \varepsilon}} + C_{1\varepsilon} \frac{\varepsilon}{k} C_{3\varepsilon} G_b + S_\varepsilon \quad (5)$$

Like the standard k- $\varepsilon$  model, values for  $\sigma_k$ ,  $\sigma_\varepsilon$ ,  $C_{1\varepsilon}$ , and  $C_{2\varepsilon}$  are user defined constants that have been found through years of experimentally collected data. However, terms such as  $C_1$  and  $S$  are not constants, but derived from higher order equations.

The k- $\omega$  turbulence is another commonly used two-term turbulence model. It is also empirically based and solves for a turbulent kinetic energy term,  $k$ . The k- $\omega$  model differs in that it solves for the specific dissipation rate of turbulent energy,  $\omega$ . This specific rate is often described as the ratio of  $\varepsilon$  to  $k$ . (Wilcox, 1999). The k- $\omega$  model incorporates modifications for low-Reynolds number effects that happen at the wall boundary. Due to these modifications, the k- $\omega$  model can more accurately predict the effects of wall bounded flows.

The third model that is examined in this study is the Reynold's stress equation model or RSM. The Reynold's stress equation model is typically regarded as a more complete turbulence

model because it takes into consideration flows with streamline curvature, flow separation, and zones with re-circulating flows (T. H. Shih, Zhu, & Lumley, 1995).

Dr. Said, Dr. Abdel-Meguid, and Dr. Rabie used each of the four turbulence models to predict the flow coefficient of a butterfly valve at different disk angles. A butterfly valve is essentially an open pipe with a flat disk that rotates to either increase or decrease volumetric flow rate. A cross-section of a butterfly valve can be seen in figure 2.2.

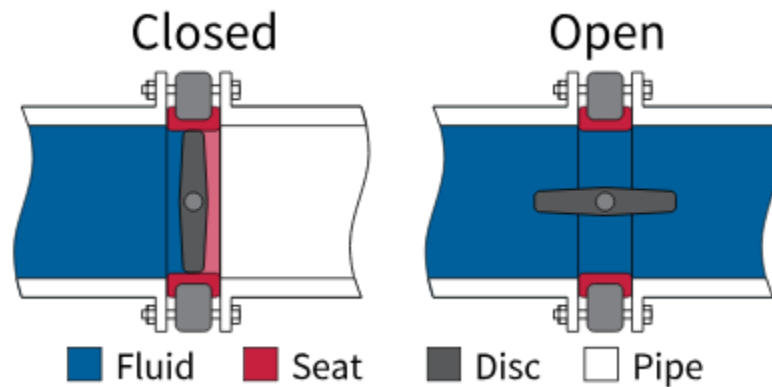


*Figure 2.2: Butterfly Valve Cross-Section*

A disk angle of  $90^\circ$  is commonly referred to as the fully open position. The disk angles analyzed in this study were  $40^\circ$ ,  $60^\circ$ , and  $70^\circ$ . All the results from each CFD simulation were compared to empirical data. The conclusion of this study was that no one turbulence model could successfully deal with all cases of disk orientation. This may be due to the large amount of turbulence created by a butterfly valve's disk mechanism as opposed to the comparatively smooth path that fluid can take through a ball valve. At each unique disk orientation, a unique turbulence model had the lowest percent difference from the experimentally determined values. The turbulence model with the lowest percent difference varied from disk orientation to disk orientation (Said et al., 2016).

Another explanation as to why no one turbulence model was the most accurate is that every turbulence model has its own advantages and disadvantages. For example, the realizable  $k-\varepsilon$  model tends to predict the spreading rate of jets and the mean flow of complex structures for flows involving rotation more accurately than the standard  $k-\varepsilon$  model. This is because the

realizable  $k-\epsilon$  model contains a new formulation for the turbulent viscosity term. In the standard  $k-\epsilon$  model this term is calculated using empirically derived constants. In the realizable  $k-\epsilon$  model this term derived from an exact equation for the transport of the mean-square vorticity fluctuation (T.-H. Shih, Zhu, & Lumley, 1993).

Although the realizable  $k-\epsilon$  model does have advantages over the standard  $k-\epsilon$  model, it is more susceptible to poor mesh and element quality. There is no one turbulence model that provides the most accurate computational results for every physical phenomenon. The results of this study can be seen in the following figures 2.3 – 2.5 which illustrate the relationship between volumetric flow-rate,  $Q$  and the square root of pressure drop. The slope of this relationship is the flow coefficient for the butterfly valve at a specific disk orientation.

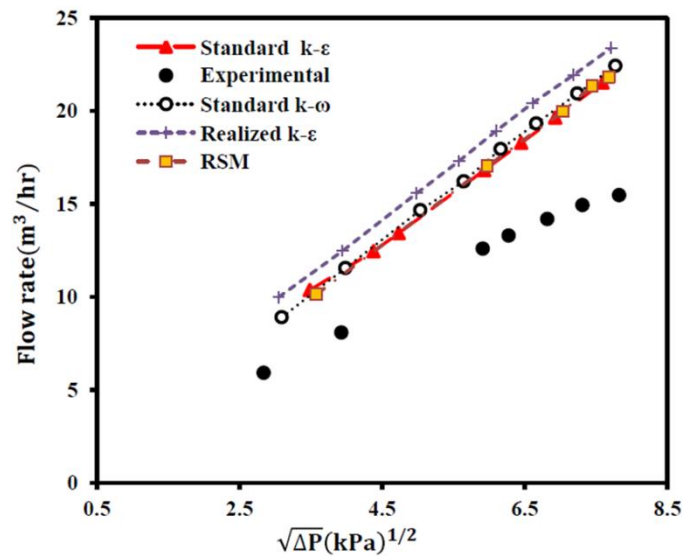


Figure 2.3: Flow Capacity at  $\theta = 40^\circ$

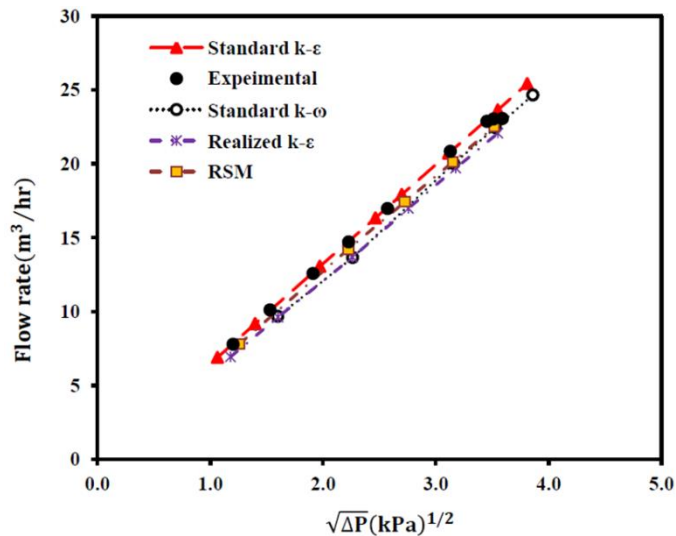


Figure 2.4: Flow Capacity at  $\theta = 60^\circ$

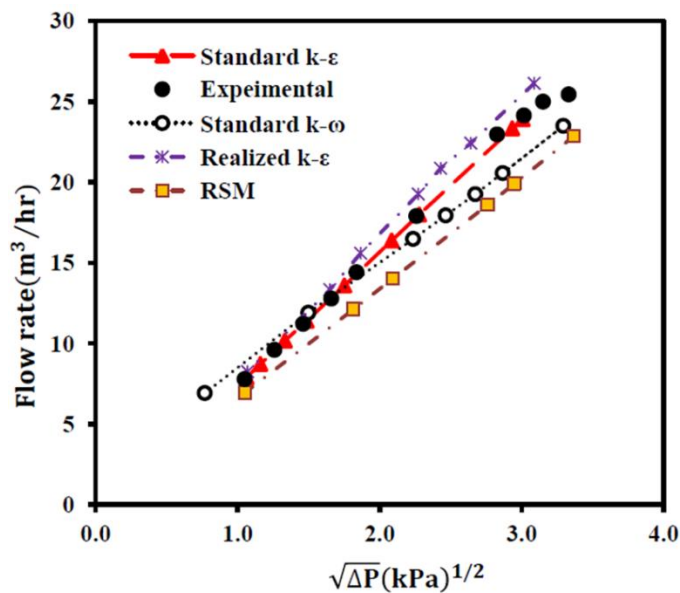


Figure 2.5: Flow Capacity at  $\theta = 70^\circ$

Dr. Said, Dr. AbdelMeguid, and Dr. Rabie recommend the development of more robust numerical solutions with different meshes and higher computational resources to minimize the discrepancies between turbulence models (Said et al., 2016).

The study published by Said, Abdel-Meguid, and Rabie, demonstrates that certain turbulence models are better suited for particular cases of fluid flow than other models. The results of this study can serve as a guide for choosing a turbulence model in the future.

### 2.3.3 Control of Volumetric Flow-Rate of Ball Valve Using V-Port

In contrast to the two previously discussed studies, an article by Dr. Chern and Wang (2004) examined a new technology in the fluid-handling industry. This new technology is the use of different profiles in ball valves. About ball valves, a profile describes the geometry of the opening in a ball. Ball valves use a rotating ball, which typically has a through hole located at the ball's center. As the ball in a ball valve is rotated the amount of flow is either increased or decreased. As previously discussed, ball valves are excellent valves for applications that require quick actuation but offer little control over volumetric flow rate. The primary focus of Chern and Wang's study is whether changing the profile of a ball, from a simple through hole to a V-shaped port, could increase the valve's control over volumetric flow rate. The authors of this study use a single turbulence model to simulate the performance of this new type of ball and compare the results to experimental data the researchers recorded.

Like the previous studies, Chern and Wang (2004) employed a CFD model that followed the governing Navier-Stokes and continuity equations. This study also used the standard  $k-\varepsilon$  model to quantify the effects of turbulence. The commercially available STAR-CD software was used for this study's computational simulations. Chern and Wang observed multiple V-port styles that varied in degree of opening. The differences between each style of V-port that was examined can be seen in figure 2.6.

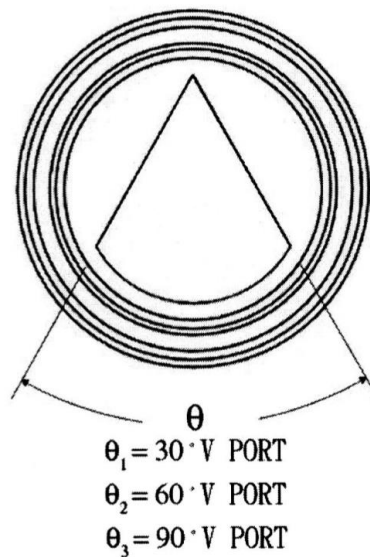


Figure 2.6: Various V-Port Designs

The authors of this study found that the geometry of the V-port had a noticeable effect on several performance characteristics other than the control over volumetric flow that the researchers were interested in observing.

The study found that the loss coefficient, flow coefficient, and cavitation index were all affected by the degree of opening of a V-port. The study also found that as the degree of opening decreases, the relationship between flow coefficient and ball position becomes linear. The relationship between a valve's loss coefficient and degree of opening is inversely proportional, as the angle of the V-port decreases, the magnitude of the loss coefficient increases (Chern & Wang, 2004). Chern and Wang explain that this phenomenon is caused by higher pressure losses that develop when fluid is forced through progressively smaller orifices.

Unlike the loss coefficient, the flow coefficient has a directly proportional relationship to the degree of opening of a V-port. As the angle of the V-port opening increases, so too does the flow coefficient. However, one important distinction between the V-port styles examined is that the 90° V-port has a non-linear relationship to the flow coefficient of a valve, whereas the other two V-port styles have a linear relationship (Chern & Wang, 2004). In fluid-handling a linear relationship between changes in valve position and volumetric flow rate are desired because it provides the user with more control and can limit hysteresis of an automated process (Cai, Braun, Laboratories, & Lafayette, 2016).

The relationship between flow coefficient and ball position can be seen in figures 2.7 – 2.9 below. Like the study conducted by Moujaes & Jagan, this study considered the effect that various Reynolds numbers have on computational results. This study found, in agreement with Moujaes & Jagan, that the effects of Reynolds number on computational results are negligible. This conclusion can also be seen in figures 2.7 – 2.9. In each of these figures the variable  $\alpha$  represents the degree of opening of the valve as it rotates from fully closed (0°) to fully open (90°). The variable  $\phi$  represents the percent openings.

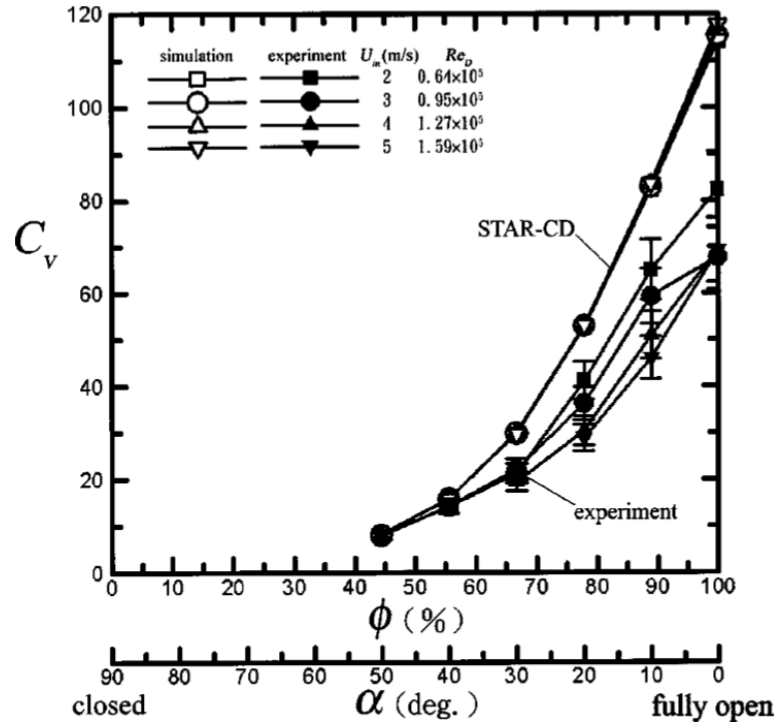


Figure 2.7: Flow Coefficient of 90° V-Port

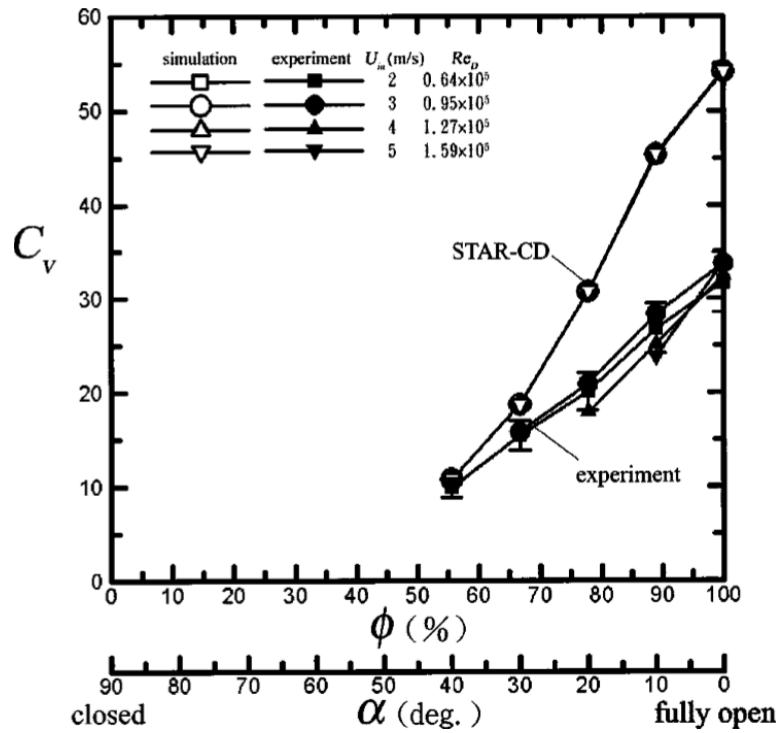


Figure 2.8: Flow Coefficient of 60° V-Port

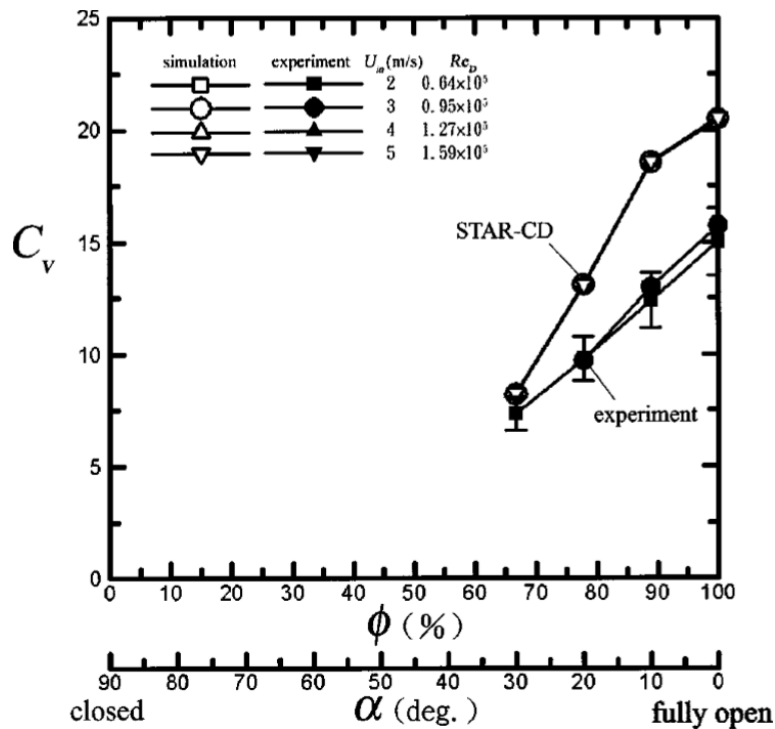


Figure 2.9: Flow Coefficient of 30° V-Port

In figure 2.10 it can clearly be seen that changing the geometry of the V-Port directly affects the relationship between flow coefficient,  $C_v$  and degree of opening,  $\alpha$ . This figure is based on experimental data collected by Chern and Wang. As the V-Port angle decreases the flow coefficient also decreases. However, as the V-Port angle increases, the relationship between flow coefficient and degree of opening becomes increasingly linear. This relationship means that both the 60° V-Port ball and 30° V-Port ball can regulate flow in a more linear manner than either the 90° V-Port ball or standard port ball

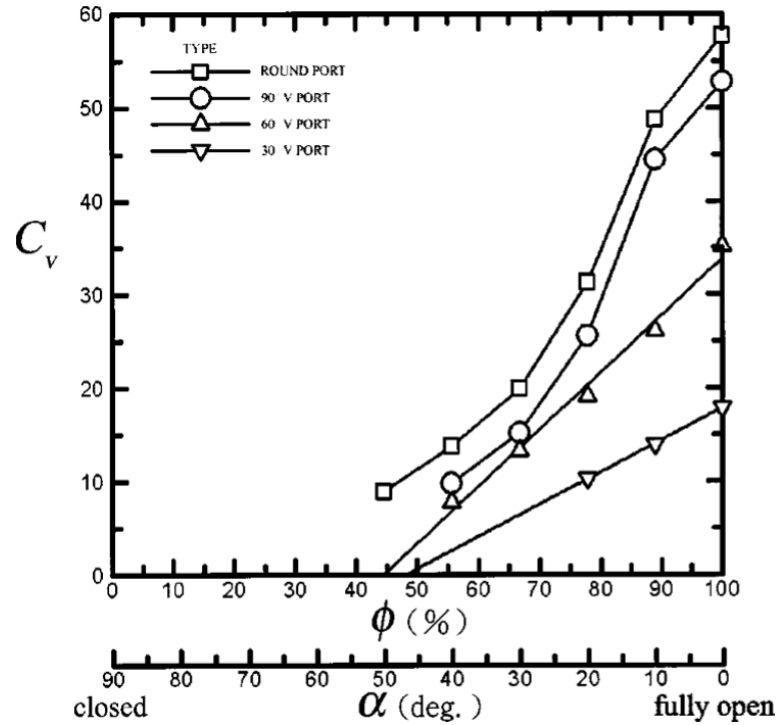


Figure 2.10: Effects of V-Ports on Flow Coefficient

Although adjusting the angle of the V-Port can create a more linear flow coefficient relationship, Chern and Wang found that it also increases the likelihood of cavitation. This study found that the cavitation index of a valve is inversely proportional to the degree of opening of a V-port. This result meant that although a 30° V-Port can linearly control the volumetric flow rate of a valve, it is also the most likely to cause cavitation (Chern & Wang, 2004). Cavitation index,  $C_s$  is defined as the ratio between the pressure drop across a valve and the differential between the inlet pressure and saturated vapor pressure. Cavitation index is commonly used in industry to describe the possibility of cavitation occurring. The formulation for cavitation index,  $C_s$  can be seen in equation (6) below.

$$C_s = \frac{\Delta P}{P_{in} - P_v} \quad (6)$$

Where:

- $\Delta P$  is the pressure drop across the valve
- $P_{in}$  is the pressure at the inlet

- $P_v$  is the saturated vapor pressure

Chern and Wang also concluded that the possibility of cavitation increases as the valve approaches its fully closed position, which is evident in figure 2.11. The data displayed in figure 2.11 was also captured experimentally. The presence of cavitation can make computational simulations more complicated and less reliable if not handled appropriately. In fluid flows where cavitation is present, a single phase CFD model is no longer adequate. A multiphase CFD model is needed to accurately model the behavior and interaction between the fluids and vapors present. For this reason, Chern and Wang's computational models only analyze degrees of opening ranging from fully open ( $0^\circ$ ) to  $50^\circ$ . The possibility of cavitation at lower degrees of opening is an important consideration to make for future studies.

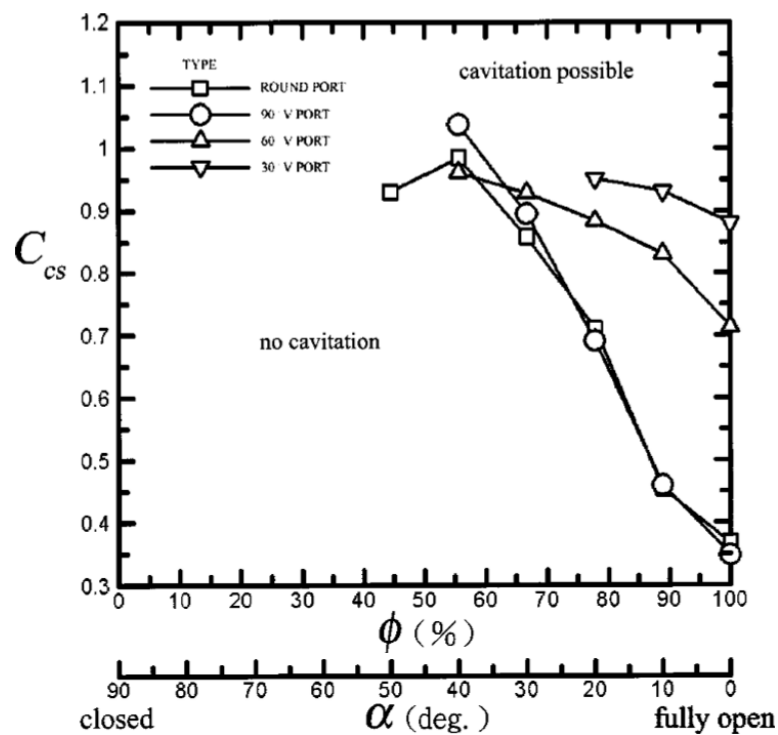


Figure 2.11: Effect of V-Ports on Cavitation Index

## 2.4 Innovation

In the fluid-handling industry there is an increasing demand for cheap valves that have quick actuation and provide a high degree of control over volumetric flow rate. Research by

Chern and Wang has demonstrated that modifying the profile of a ball valve can increase control over volumetric flow rate but can also lead to cavitation and affect the reliability of a computational model.

In industry today, an entirely new mechanism for regulating flow within ball valves is being developed. Instead of a ball with either a through hole or V-port, designing a ball with an outside groove, which opens as a valve is actuated, can be used to increase the control a ball valve has over volumetric flow rate by greater amounts than either the traditional ball or V-port ball.

There exists the need for a study that examines multiple computational fluid dynamic models, verifies the results through experimental data, and quantifies the performance characteristics of this entirely new type of valve. The completion of this suggested study would allow future researchers to study how the increased control over volumetric flow rate minimizes hysteresis within a fluid-handling system.

## 2.5 Summary

As previous studies have shown computational fluid dynamics is a powerful tool in the both the development and examination of new fluid handling devices. Crucial to the success and validity of any CFD based analysis is the verification of analytical data with experimental data. These previous studies have laid a viable framework to develop and analyze new technologies in the fluid handling industry.

## CHAPTER 3. RESEARCH METHODOLOGY

This chapter will cover research methods, framework, and analysis methods used in this study.

### 3.1 Research Framework

The research framework used in this study is very similar to the studies previously mentioned. The commercially available CFD software package, FLUENT, was used to investigate the interactions between the moving fluid and structures in a valve. A simple circuit was constructed to collect experimental data. Unlike previous studies, this study analyzed a new type of bottom-load ball, which has an outside groove that expands as it is rotated. Previous studies have analyzed the effects of manipulating the profile of the orifice in a ball valve, but none have observed the effects of an outside groove (Chern & Wang, 2004).

The type of research that was conducted was a computational study followed by an experimental study to validate any computational results. The nature of this research is quantitative. Quantifying the relationship between the position of the ball, in a ball valve, and volumetric flow rate is the desired outcome of this research. The position of the ball was measured in degrees. Along with volumetric flow rate, this study will quantify the relationship between the degree of opening of three bottom load ball valve designs and several performance characteristics of a ball valve such as flow coefficient and cavitation index.

### 3.2 Testing Methodology

There was no sampling approach for the CFD analysis of this study. This is because all CFD software packages provide a numerical approximation to a set of equations, typically the Navier-Stokes equations (Hoffman & Johnson, 2007). Assuming the design of the ball is held constant, and all boundary conditions of the simulation are held constant, the numerical approximation will be the same for any iteration.

However, this study did analyze the rate of convergence among simulations. In numerical methods such as computational fluid dynamics or finite element analysis, the number of individual elements can affect the value of numerical approximations (Hutton, 2004). As the

number of elements grow, a simulation approximation becomes more accurate. When increasing the number of elements in a simulation no longer changes the numerical approximation, a simulation is considered to have converged.

This study has several variables and units of measurement. The primary independent variable in this study was the position of the ball. The position of ball was measured in degrees from the fully closed position. The primary dependent variable was volumetric flow rate. Volumetric flow rate was measured in U.S. gallons per minute (GPM). The other dependent variable measured in this study was pressure at the inlet and outlet of the valve. Pressure was measured in pounds per square inch (PSI).

Flow coefficient and cavitation index were the two performance characteristics that were calculated from the resulting dependent variables. Unlike the CFD portion of this study, the physical experimentation portion required multiple measurement instruments. The two primary measurement instruments were a flowmeter and pressure transducers. All changes in flow rate and pressure drop due to the valve's position were manually recorded.

### 3.3 Summary

This chapter summarized the proposed methodology for the study to be conducted. Additionally, it defined the performance characteristics to be analyzed and quantified by both a computational fluid dynamic simulation and experimental data.

## CHAPTER 4. RESULTS

### 4.1 Computational Analysis

The following sections describe the procedure for developing a computational fluid dynamic model. The following sections also describe the outcome of each computational simulation conducted in this study.

#### 4.1.1 Fluid Domain Creation

As discussed in chapter two, computational fluid dynamic software differs from finite element analysis in that the empty volume, where fluid flows, is the geometry that is discretized. In a finite element analysis, the solid material is discretized. To develop a 3D model for the computational simulations, the commercially available CAD program Inventor was used. The three bottom-load ball designs that are the subject of this study all share a common valve body. The valve is a bottom-load ball valve with 1.5-inch diameter ports at the inlet and outlet. A half-section view of this bottom-load ball valve can be seen in figure 4.1. The ball design in figure 4.1 is the standard port ball design.

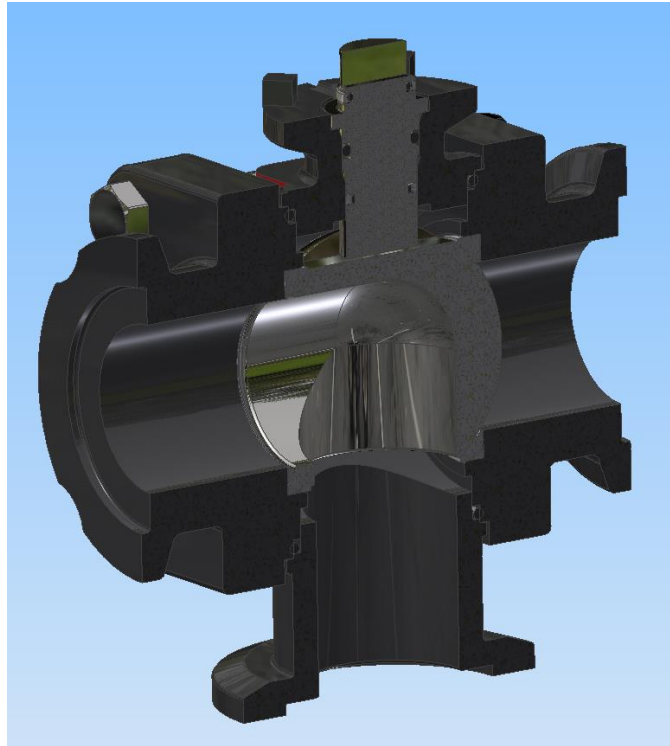


*Figure 4.1: Half-Section of Bottom-Load Ball Valve*

A 3D CAD part was then created to fill in the empty space found in the bottom-load ball valve shown above in figure 4.1. A unique 3D model, that represented the empty space in the valve, was created for each ball design. For every degree of opening that a computational simulation was conducted, a unique 3D model was created. In total, 18 unique 3D models were created to analyze each ball design's performance. In figure 4.2 it can be seen how one of the 3D models, that represents the fluid domain, fills the empty space in the bottom-load ball valve. The 3D model in figure 4.2 represents the fluid domain of the standard port ball at its fully open position.

In figure 4.2 it can also be seen that the 3D model does not represent every single empty space that fluid can flow through. The small volumes that are not represented by each 3D model were purposefully omitted for meshing concerns that will be discussed in greater detail in section 4.1.2. The metric for determining which small volumes were omitted is also discussed in section 4.1.2.

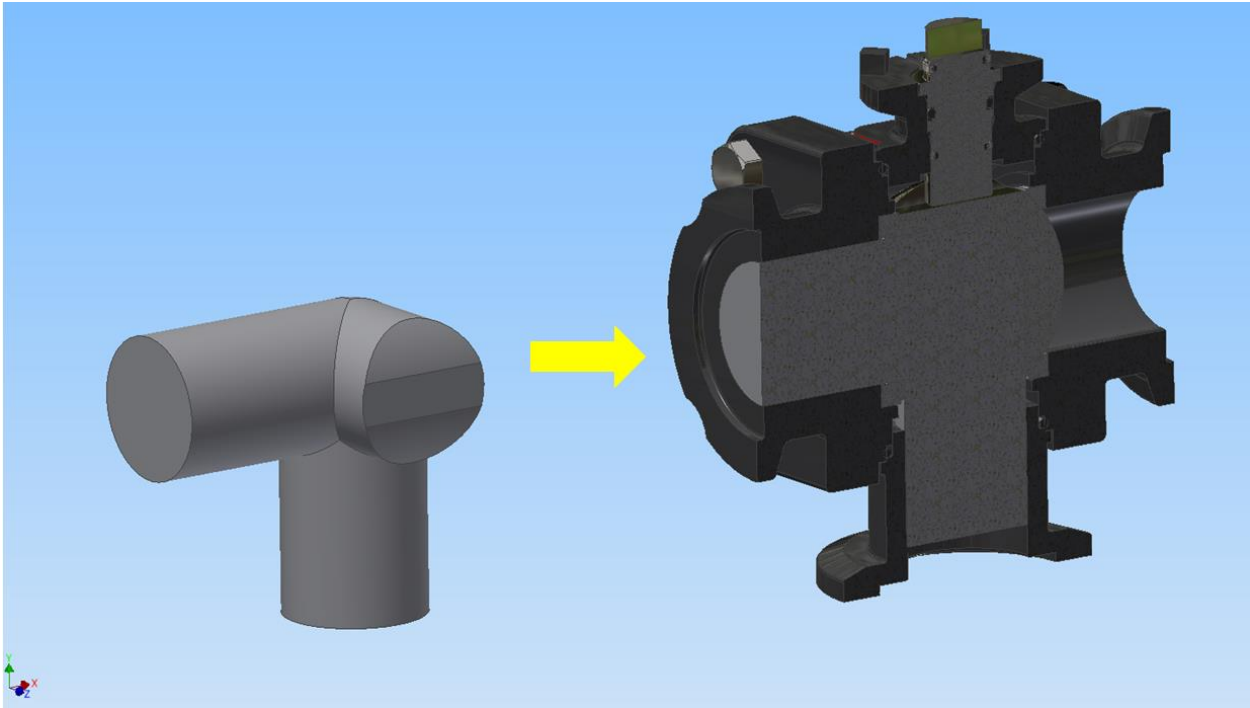


*Figure 4.2: 3D model of Fluid Domain for Standard Ball Design*

#### 4.1.2 Meshing

Meshing is a crucial step in any computer aided engineering (CAE) process. In the meshing process, a continuous volume undergoes the process of discretization where it is modeled as discrete volumes of known dimensions. Meshing also plays a critical role in the accuracy and reliability of a CFD model. As discussed in chapter two, certain turbulence models require meshes of varying quality. In this study several meshes of varying quality were analyzed and used to conduct computational simulations. By comparing the deviation of computational results from physical data, an estimate for the minimum mesh quality was obtained.

In figure 4.3 below a mesh of the standard ball at its fully open position can be seen. This mesh was used to conduct a computational simulation. The mesh had 214,028 elements with an average element size of 0.125 inches. Most elements used in this study are tetrahedrons. Elements that are not tetrahedrons are hexagons.

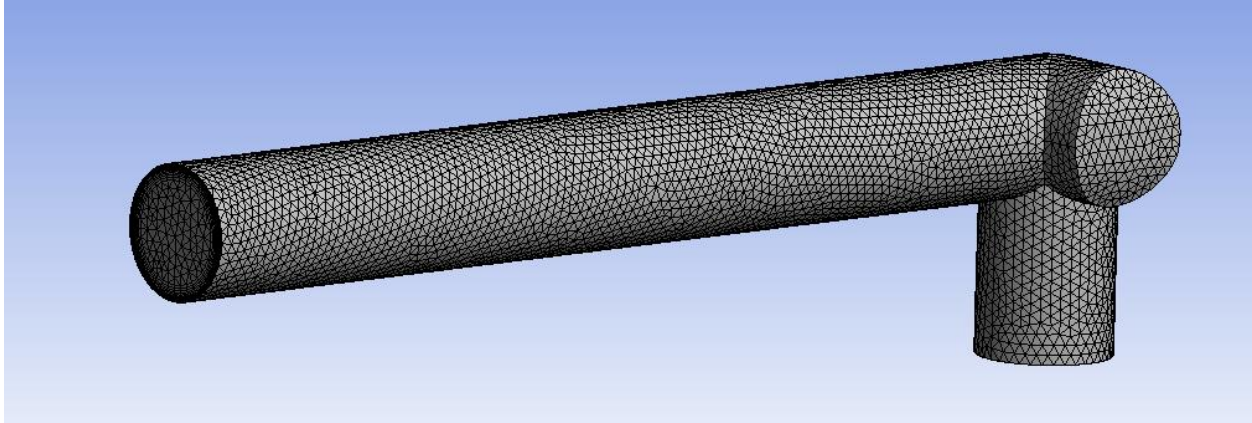


Figure 4.3: Mesh of Standard Ball at Fully Open Position

Element skewness was the primary metric used to determine mesh quality before a computational simulation was conducted. Element skewness refers to how close an element or cell is to be the ideal equilateral or equiangular. For example, a quadrilateral element composed of all 90° corners would have low skewness and good cell quality. Values of skewness for 3D elements are defined by equation (7) below.

$$\text{Skewness} = \frac{\text{Optimal Cell Size} - \text{Cell Size}}{\text{Optimal Cell Size}} \quad (7)$$

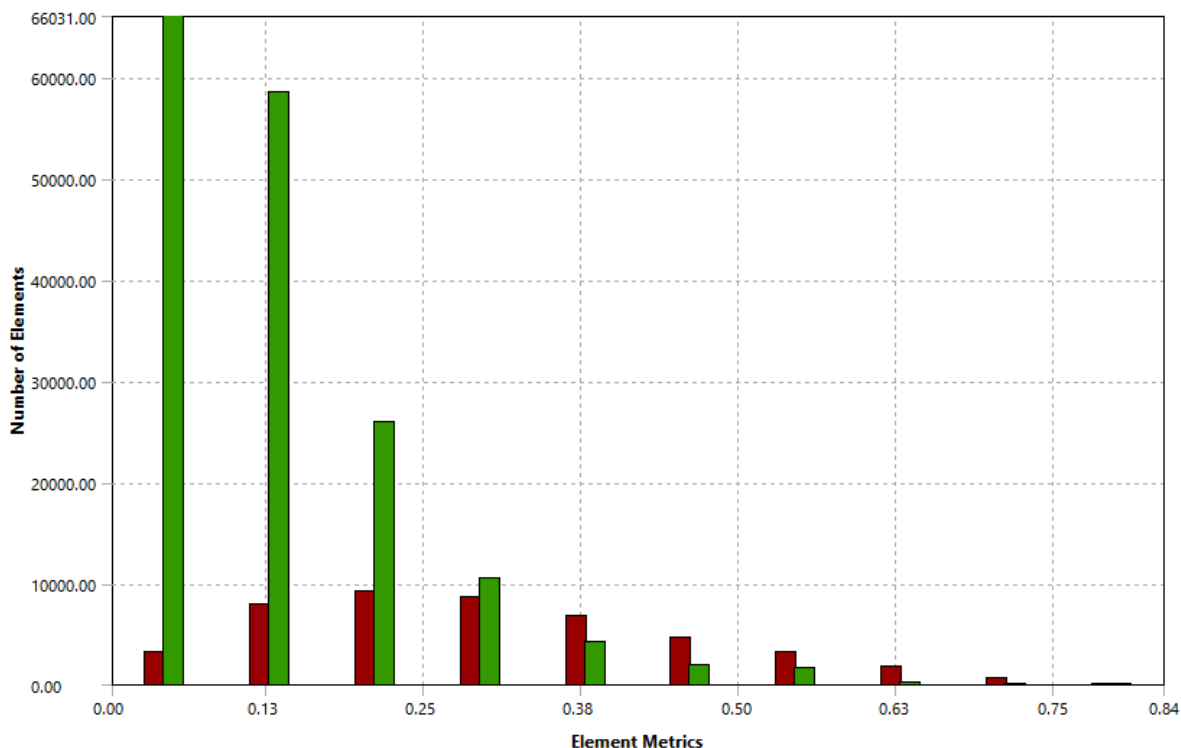
The equation above is how FLUENT quantifies skewness in its CFD software. FLUENT also provides a general guideline as to what skewness values constitute good or poor cell quality. The general guideline can be seen below in table 4.1.

Table 4.1: Skewness and Corresponding Cell Quality

Value of Skewness	Cell Quality
1	Degenerate
0.9 – < 1	Bad
0.75 – 0.9	Poor
0.5 – 0.75	Fair
0.25 – 0.5	Good
>0 – 0.25	Excellent
0	Equilateral

High skewness can affect the convergence, accuracy, and run time of a CFD simulation. This is because all equations in the finite volume method are discretized using the distance between centroids of adjacent elements. A CFD solver assumes that the vector joining these centroids is perpendicular to the shared edge (2D element) or shared face (3D element). As skewness increases, error grows due to this assumption (Ghoreyshi, Bergeron, Seidel, Lofthouse, & Cummings, 2015).

As mentioned in section 4.1.1, there were small volumes of the fluid domain that were purposefully omitted in each 3D model. These small volumes caused the FLUENT mesher to create elements of bad cell quality or that were degenerate. Figure 4.4 illustrates the number of elements and the average skewness value for the elements in the mesh shown in figure 4.3.



*Figure 4.4: Skewness Metrics for Standard Ball Mesh (Coarse)*

Most elements are of excellent to fair quality. There are several other mesh metrics used to quantify mesh quality. However, for the scope of this study only skewness was considered for its effects on the computational results.

The estimation of a minimum mesh quality and density was found by using the mesh in figure 4.3 and the mesh shown in figure 4.5 to complete a computational simulation. Both meshes had identical boundary conditions and used the same turbulence model. The only difference between the meshes was the mesh shown in figure 4.5 is twice as fine as the mesh shown in figure 4.3. This finer mesh has an average element size of 0.0625 inches.

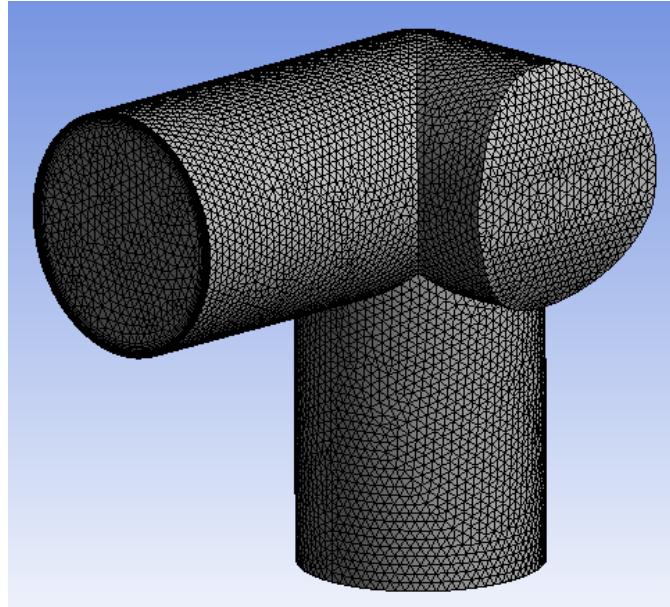


*Figure 4.5: Fine Mesh of Standard Ball at Fully Open Position*

The number of elements and the average skewness value for the elements in this fine mesh are displayed in figure 4.6.

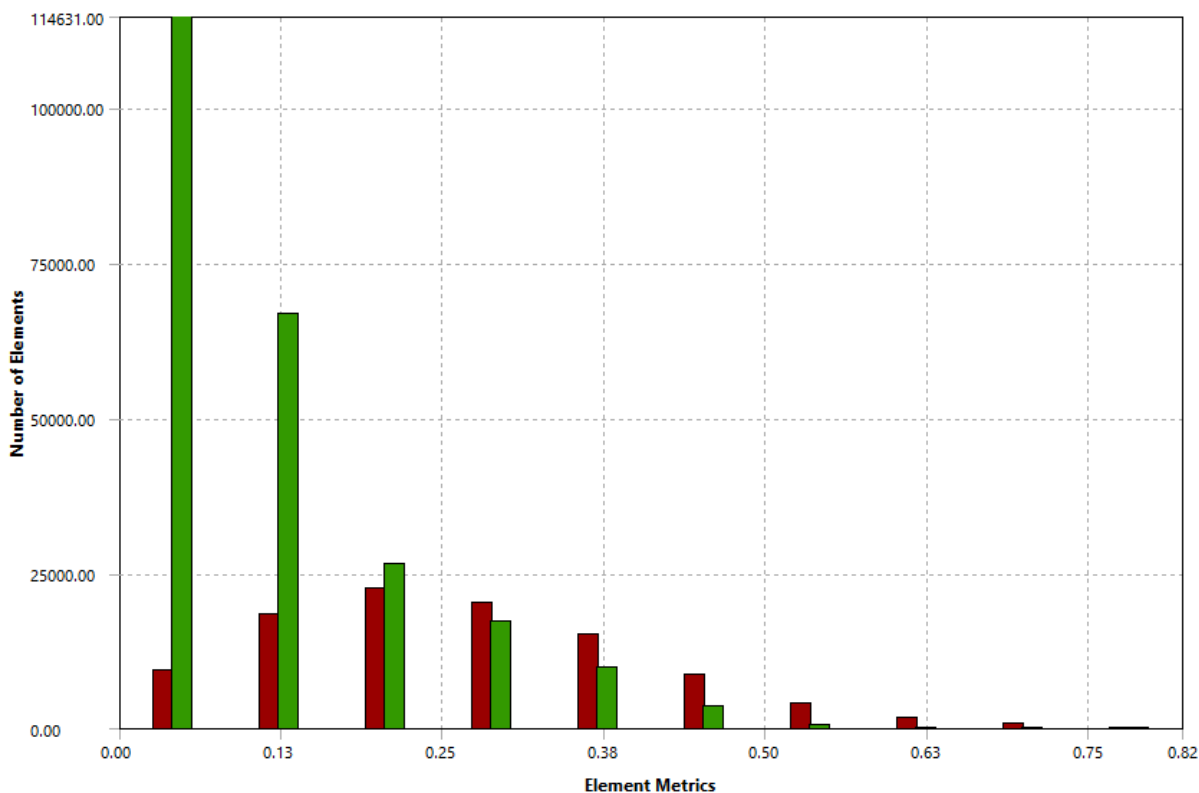


*Figure 4.6:* Skewness Metrics for Standard Ball Mesh (Fine)

Again, most of the elements in the fine mesh are of excellent quality. The results from the computational simulation showed that the coarser mesh over-predicted the flow coefficient of the standard ball at its fully open position by approximately 23.5%; this comparison is based on the calculation of flow coefficient from experimental data shown in section 4.2. The finer mesh over-predicted flow coefficient by approximately 18.7%. Although the finer mesh has a lower percent difference than the coarse mesh, the improvement in accuracy is marginal. The comparison between the two meshes can be seen in table 4.2. Other factors that influence a CFD model's accuracy will be discussed in the following sections.

*Table 4.2:* Mesh Comparison

Mesh	Element Size (inch)	No. of Elements	Computational Flow Coefficient, $C_v$	Experimental Flow Coefficient, $C_v$	Percent Difference
Coarse	0.125	214,028	51	41.3	23.5%

Table 4.2: Continued

Fine	0.0625	338,572	49	41.3	18.7%
------	--------	---------	----	------	-------

### 4.1.3 Y+ Boundary Layer

When attempting to model the behavior of fluids, particularly at the wall boundary, having a fine mesh alone is not adequate. As fluids approach the wall boundary, flow transitions from relatively higher Reynolds number to what is commonly referred to as low Reynolds number flow. This is due to the viscous forces at the wall boundary overcoming the inertial forces present throughout the rest of the fluid domain. The overall flow found in the fluid domain may be turbulent (high Reynolds number), but as its flow approaches what is called the viscous sublayer it transitions into relatively laminar flow. The velocity of fluid decreases until it reaches a velocity of zero at the wall boundary.

To model this phenomenon, a very fine mesh must be present near the wall boundary. This mesh is often referred to as a boundary layer or inflation layer. The metric used to quantify the necessary size of this inflation layer is known as the  $y^+$  value. The equation for  $y^+$  can be seen below in equation (8).

$$y^+ = \frac{yu_t}{\nu} \quad (8)$$

Where:

- $y$  is the distance of a cell to the wall
- $u_t$  is the friction velocity
- $\nu$  is the kinematic viscosity

Typically,  $y^+$  values necessary to model fluid flow behavior between the viscous sublayer and the wall boundary are 0 – 1. As the distance from the wall increases, the minimum  $y^+$  value increases. As fluid flow transitions from the viscous sublayer, where viscous forces overcome inertial forces, to the buffer layer the necessary  $y^+$  value is approximately seven. The approximations of  $y^+$  have been found through various studies throughout the years (Salim & Cheah, 2009).

The CFD software FLUENT provides a tool for automatically creating an inflation layer for a given mesh. In this tool the total height of the inflation layer in number of cells is specified. For the meshes in this study a total height of fifteen cells was used. The cell at the wall boundary has a  $y^+$  value of 1. FLUENT requires the user to specify a growth rate for the neighboring cells in the inflation layer. The growth rate in this study was the default 0.252, meaning every cell after the first layer has a height that was 25.2% bigger than the preceding cell. An image of this inflation layer at the outlet can be seen below in figure 4.7.

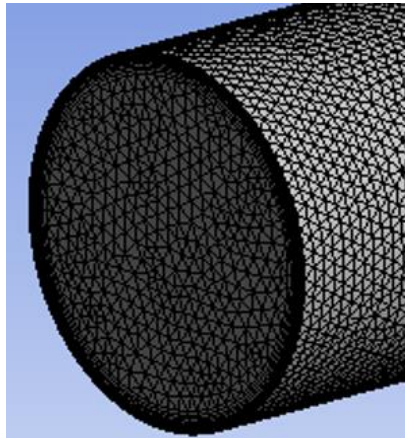


*Figure 4.7: Inflation Layer at Mesh Outlet*

#### 4.1.4 Boundary Conditions & Simulation Settings

The boundary conditions of this study were created to accurately depict the physical conditions each ball valve design experienced. Perhaps the most impactful boundary condition was the velocity of the fluid at the inlet. This condition was found by converting the volumetric flow rate found from physical experimentation and solving equation (9) for velocity. The CFD model solves for dependent variables such as pressure drop, velocity profile, turbulent energy, etc. from specifying the velocity at the inlet.

$$V = \frac{Q}{A} \quad (9)$$

Where:

- $Q$  is the volumetric flow-rate at the inlet
- $A$  is the cross-sectional area of the inlet

Another boundary condition that affected the computational results of this study was the pressure at the outlet of the ball valve. For all simulations an outlet pressure of 0 PSI was specified. The boundary condition for the walls in this study were that the walls were rigid, experienced no deflection, had no slip at the wall, and had a roughness constant of 0.5, which is the default value specified by FLUENT. The no slip condition signifies that the fluid at the wall moves with the same velocity as the wall. Because the wall is modeled as a rigid and stationary wall, the fluid at the wall boundary has a velocity of zero.

FLUENT requires that a computational simulation be defined as a transient model or steady state model. For this study all CFD models were solved under the steady state condition. Steady state models are appropriate to use in flows where the characteristics of flow do not change with time. Most practical flows can be assumed to have reached a steady state after an initial unsteady flow development stage passes.

In this study, a steady state is assumed to have been reached after the pump begins to push fluid through the bottom-load ball valves. The short time between the pump starting and fluid beginning to flow through the bottom-load ball valve would be the unsteady state of this study. However, the scope of this study only concerns the flow coefficient of three ball valve designs after fluid has already begun traveling through each design and a steady state has been reached.

The steady state assumption made in the computational portion of this study also represents the experimental procedure more accurately than the transient or unsteady assumption. In the experimental procedure the pump runs for some time until the flow-meter reads a steady volumetric flow rate and the pressure transducers read steady pressures.

#### 4.1.5 Fluid Properties

The fluid properties of this study are that of water at 60°F. From this assumption other fluid properties such as the saturated vapor pressure of water were determined. Using readily available phase diagrams, it was found that the saturated vapor pressure for water at 60°F is 0.256 PSI. The saturated vapor pressure of water was used to determine the cavitation index of

each ball valve design at various degree of opening positions. The specific gravity of water at 60°F is one. This specific gravity value was used in the calculation of flow coefficient.

#### 4.1.6 Turbulence Models

As discussed in chapter two, the turbulence model of a computational simulation can affect the results by a considerable amount. In this study two different turbulence models were used and compared. The first model that was used to analyze the three ball designs was the standard k- $\epsilon$  model. As discussed in chapter two this model is a two-term semi-empirical model. It was also used as the model when determining an appropriate element size for the meshes in this study.

The other model used in this study was the transition SST model. The transition SST model was developed by coupling the k- $\omega$  transport equations with two other transport equations. The transition SST model is a four-equation model, unlike the two-equation standard k- $\epsilon$  model. The benefit of the transition SST model is that it changes which transport equations are solved depending on the distance of a cell to the wall.

In the inner region of the inflation layer, the model uses the k- $\omega$  transport equations to model flow all the way down to the viscous sublayer. At the outer layers of the inflation layer and close to the free stream area of flow, the transport equation changes to one for intermittency. A transport equation for transition onset criteria determines when the transition between equations occurs (Menter, Langtry, Völker, & Huang, 2005). The four transport equations for the transition SST model are shown below in equations (10) – (13).

$$\frac{\partial(\rho k)}{\partial t} + \frac{\partial(\rho u_j k)}{\partial x_j} = \hat{P}_k - \hat{D}_k + \frac{\partial}{\partial x_j} \left[ (\mu + \sigma_k \mu_t) \frac{\partial k}{\partial x_j} \right] \quad (10)$$

$$\frac{\partial(\rho \omega)}{\partial t} + \frac{\partial(\rho u_j \omega)}{\partial x_j} = P_\omega - D_\omega + \frac{\partial}{\partial x_j} \left[ (\mu + \sigma_\omega \mu_t) \frac{\partial \omega}{\partial x_j} \right] + 2(1 - F_1) \frac{\rho \sigma_{\omega 2}}{\omega} \frac{\partial k}{\partial x_j} \frac{\partial \omega}{\partial x_j} \quad (11)$$

$$\frac{\partial(\rho \gamma)}{\partial t} + \frac{\partial(\rho u_j \gamma)}{\partial x_j} = P_\gamma - E_\gamma + \frac{\partial}{\partial x_j} \left[ \left( \mu + \frac{\mu_t}{\sigma_f} \right) \frac{\partial \gamma}{\partial x_j} \right] \quad (12)$$

$$\frac{\partial(\rho\widehat{Re}_{\theta t})}{\partial t} + \frac{\partial(\rho u_j \widehat{Re}_{\theta t})}{\partial x_j} = P_{\theta t} + \frac{\partial}{\partial x_j} \left[ \sigma_{\theta t} (\mu + \mu_t) \frac{\partial \widehat{Re}_{\theta t}}{\partial x_j} \right] \quad (13)$$

As stated in section 4.1.2, the standard k- $\epsilon$  model was used as a tool to estimate minimum element size. The results of those simulations are outlined in table 4.2. The flow coefficient predicted by the standard k- $\epsilon$  model was approximately 18.7% higher than the experimental flow coefficient.

For the same given mesh, a computational simulation using the transition SST model was conducted. The computational flow coefficient using the transition SST model was only 0.99% higher than the experimental flow coefficient. These flow coefficients and percent differences compare the standard ball design at its fully open position. The comparisons between turbulence models can be seen in table 4.3. The advantages of using the transition SST model are the primary reasons that it was chosen as the turbulence model for the remainder of this study. The following section will outline the results obtained from all computational simulations using the transition SST model to capture the effects of turbulence.

*Table 4.3: Comparison of Turbulence Models*

Degree of Opening	Element Size (in)	Turbulence Model	Pressure Drop, $\Delta P$ , PSI	Computational Flow Coefficient, $C_v$	Experimental Flow Coefficient, $C_v$	Percent Difference
90°	0.125	Standard k- $\epsilon$	9.23	51.0	41.3	23.50%
90°	0.0625	Standard k- $\epsilon$	10.01	49.0	41.3	18.70%
90°	0.0625	Transition SST	13.83	41.7	41.3	0.99%

#### 4.1.7 Result Interpretation

##### 4.1.7.1 Standard Ball Design

The results of all 6 computational simulations for the standard ball design can be seen in table 4.4 below. The data from table 4.4 was plotted to show the relationship between flow coefficient and degree of opening. This relationship is illustrated in figure 4.8 below and clearly demonstrates the non-linear relationship between flow-coefficient and degree of opening. Figure 4.9 below demonstrates that a design with a non-linear flow-coefficient curve will increase volumetric flow-rate non-linearly as the ball rotates from closed to open positions.

Table 4.4: Computational Analysis of Standard Ball

Degree of Opening	Pressure Drop, $\Delta P$ , PSI	Volumetric Flow-Rate, $Q$ , GPM	Computational Flow Coefficient, $C_v$	Experimental Flow Coefficient, $C_v$	Percent Difference
90°	13.83	155	41.69	41.28	0.99%
75°	13.85	149	40.04	39.00	2.66%
60°	16.63	139	34.08	30.85	10.47%
45°	27.71	109	20.71	18.64	11.10%
30°	67.00	53.1	6.49	7.68	15.49%
15°	44.90	20.2	3.01	2.91	3.44%

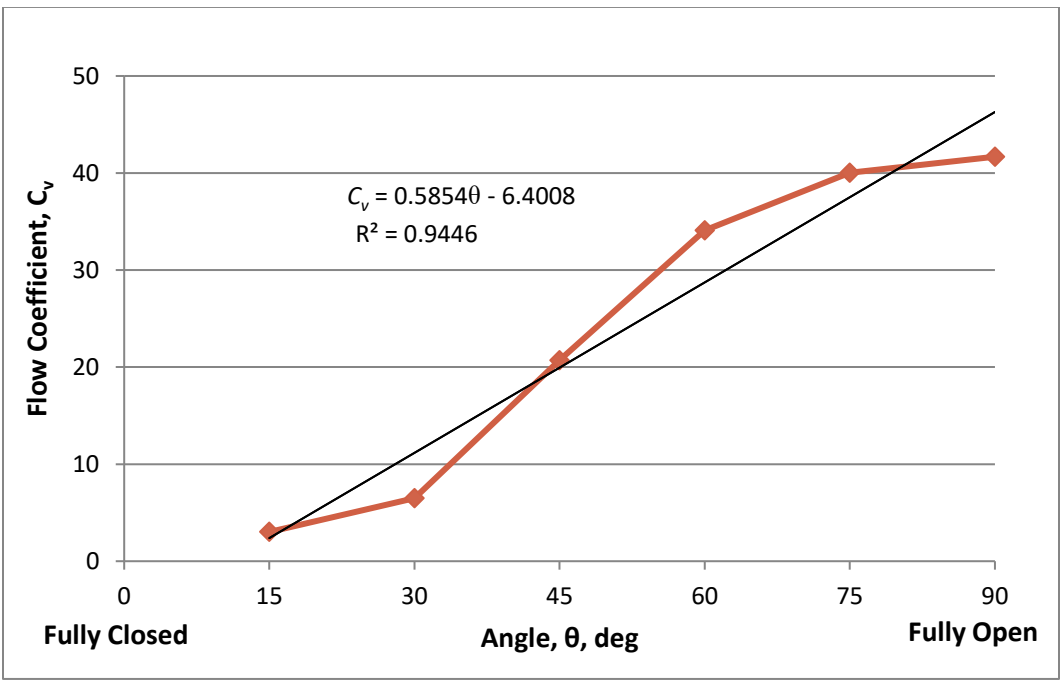


Figure 4.8: Flow-Coefficient vs. Degree of Opening (Standard Ball)

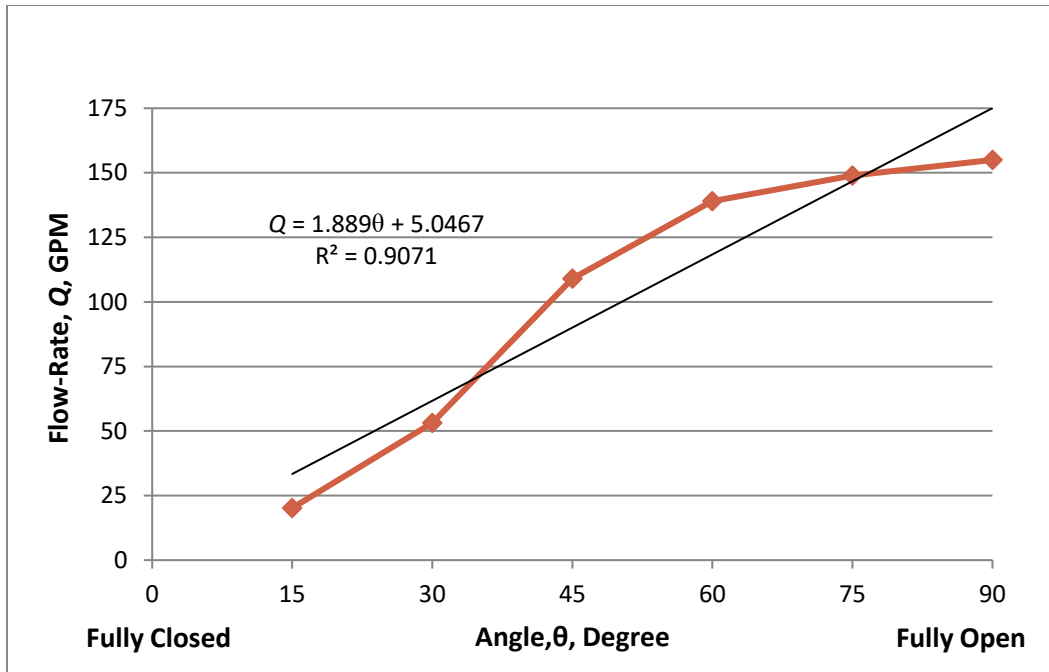


Figure 4.9: Volumetric Flow-Rate vs. Degree of Opening (Standard Ball)

As can be seen by the percent difference values in table 4.4, the computational simulation tends to predict flow coefficient most accurately in flows that exhibit relatively less turbulence. As the degree of opening decreases, the turbulence created becomes more complex and difficult to model. To accurately capture increasingly complex turbulence, a progressively finer mesh would be required.

However, the last data point for percent difference in table 4.4 reverses the trend of percent difference increasing as degree of opening decreases. This may be due to the presence of cavitation. In figure 4.10 below, one can see that the cavitation index of the standard ball design is at its highest at the degree of opening nearest the fully closed position. The computational model may only be over-predicting flow coefficient by 3.44% as a coincidence rather than accurately modeling the physical phenomena occurring. To accurately model fluid flows with cavitation present, a multiphase CFD model must be developed as discussed in chapter two.

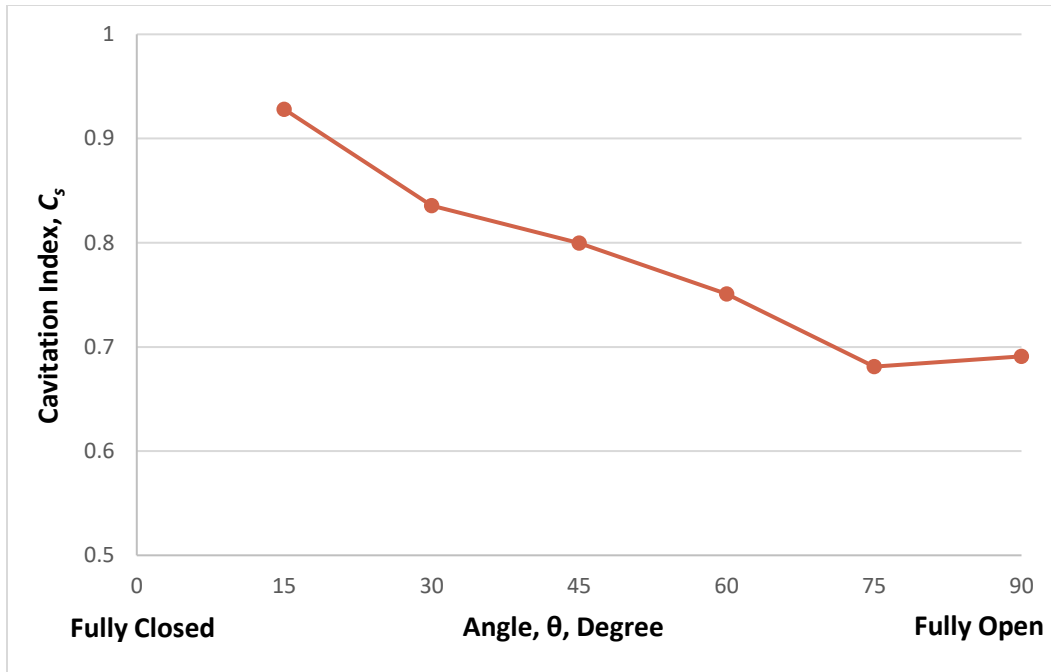


Figure 4.10: Cavitation Index vs. Degree of Opening (Standard Ball)

#### 4.1.7.2 1<sup>st</sup> Ball Design Iteration

The results of all 6 computational simulations for the first ball design iteration can be seen in table 4.5 below. The data from table 4.5 was plotted to show the relationship between flow coefficient and degree of opening. This non-linear relationship is illustrated in figure 4.11 below. Figure 4.12 below demonstrates that a design with a non-linear flow-coefficient curve will increase volumetric flow-rate non-linearly as the ball rotates from closed to open positions.

Table 4.5: Computational Analysis of 1<sup>st</sup> Ball Design Iteration

Degree of Opening	Pressure Drop, $\Delta P$ , PSI	Volumetric Flow-Rate, $Q$ , GPM	Computational Flow Coefficient, $C_v$	Experimental Flow Coefficient, $C_v$	Percent Difference
180	9.32	162	53.07	51.88	2.29%
150	9.16	158	52.20	48.26	8.16%
120	20.74	148	32.50	27.29	19.09%
90	22.41	104	21.97	17.93	22.53%
60	26.59	77	14.93	11.61	28.59%
30	49.09	51	7.28	7.53	3.32%

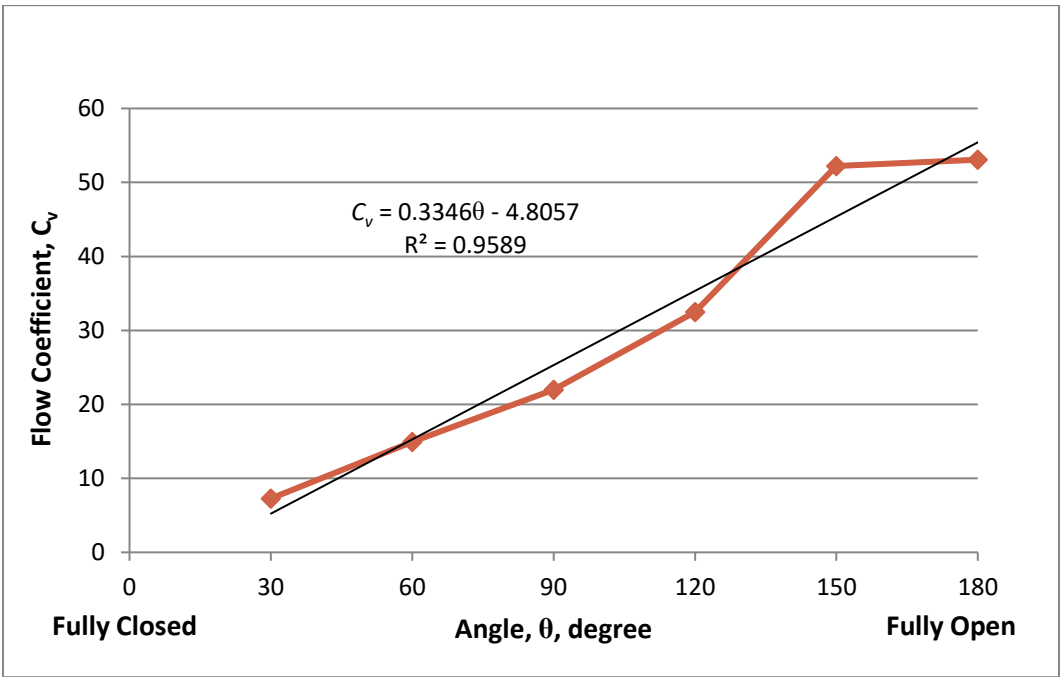


Figure 4.11: Flow Coefficient vs. Degree of Opening (1<sup>st</sup> Ball Design)

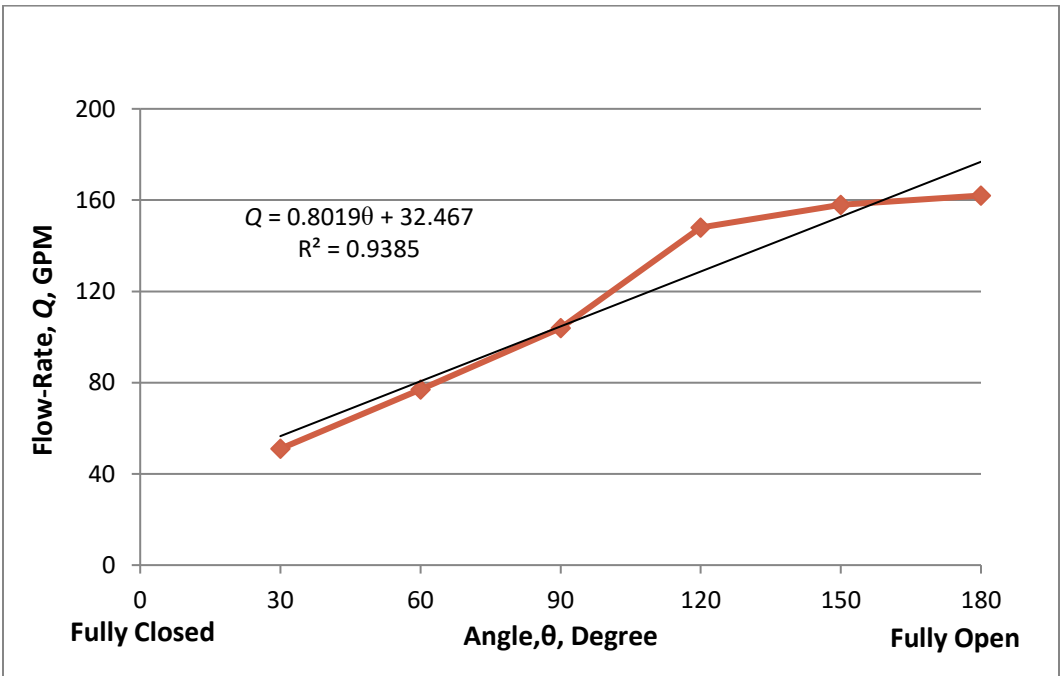
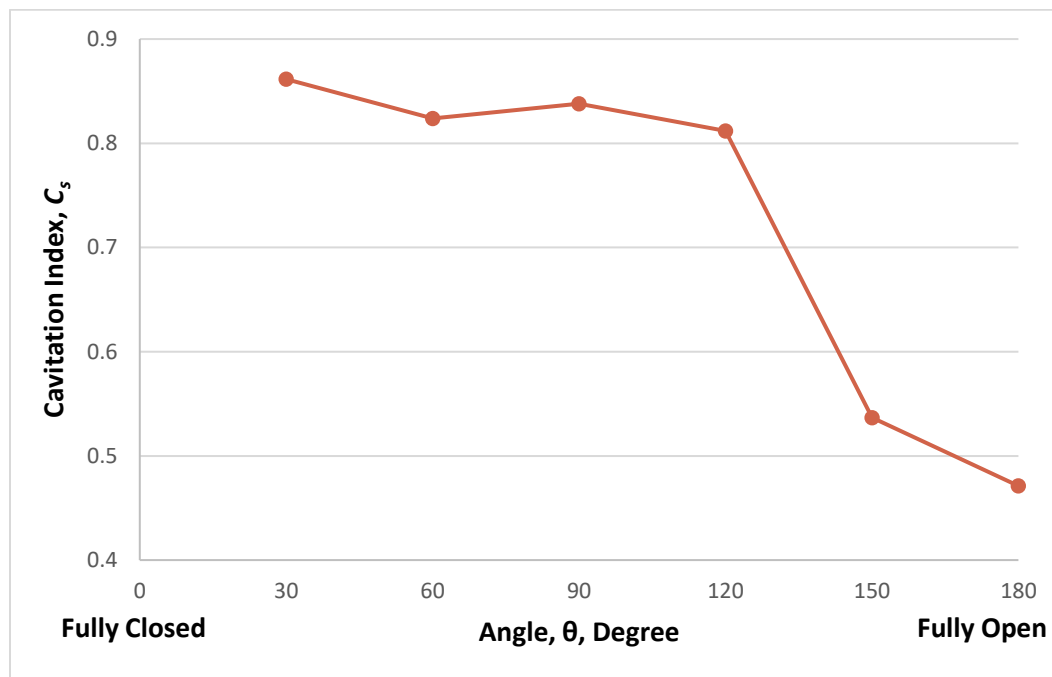


Figure 4.12: Volumetric Flow-Rate vs. Degree of Opening (1<sup>st</sup> Ball Design)

Like the CFD model developed for the standard ball, the computational simulations for the first ball design tend to predict flow coefficient most accurately in uninterrupted flows that exhibit relatively less turbulence.

Again, the last data point for percent difference in table 4.5 reverses the trend of percent difference increasing as degree of opening decreases. In figure 4.13 below, one can see that the cavitation index of the first ball design is at its highest at the degree of opening nearest the fully closed position. The computational model may only be over-predicting flow coefficient by 3.32% as a coincidence rather than accurately modeling the physical phenomena occurring. This matches what was seen in the analysis of the standard ball.



*Figure 4.13: Cavitation Index vs. Degree of Opening (1<sup>st</sup> Ball Design)*

#### 4.1.7.3 2<sup>nd</sup> Ball Design Iteration

The results of all 6 computational simulations for the second ball design iteration can be seen in table 4.6 below. The data from table 4.6 was plotted to show the relationship between flow coefficient and degree of opening. Unlike the standard ball and the first ball design iteration, the second ball design features a more linear relationship between flow coefficient and degree of opening. This linear relationship is illustrated in figure 4.14 below. Figure 4.15 below

demonstrates that a design with a linear flow-coefficient curve will increase volumetric flow-rate linearly as the ball rotates from closed to open positions.

*Table 4.6: Computational Analysis of 2<sup>nd</sup> Ball Design Iteration*

Degree of Opening	Pressure Drop, $\Delta P$ , PSI	Volumetric Flow-Rate, $Q$ , GPM	Computational Flow Coefficient, $C_v$	Experimental Flow Coefficient, $C_v$	Percent Difference
180°	6.61	162	63.01	50.5	24.77%
150°	7.48	154	56.31	41.79	34.74%
120°	12.55	136	38.39	28.70	33.76%
90°	20.72	99	21.75	16.05	35.51%
60°	38.40	62	10.01	9.31	7.52%
30°	80.55	27	3.01	4.01	24.94%

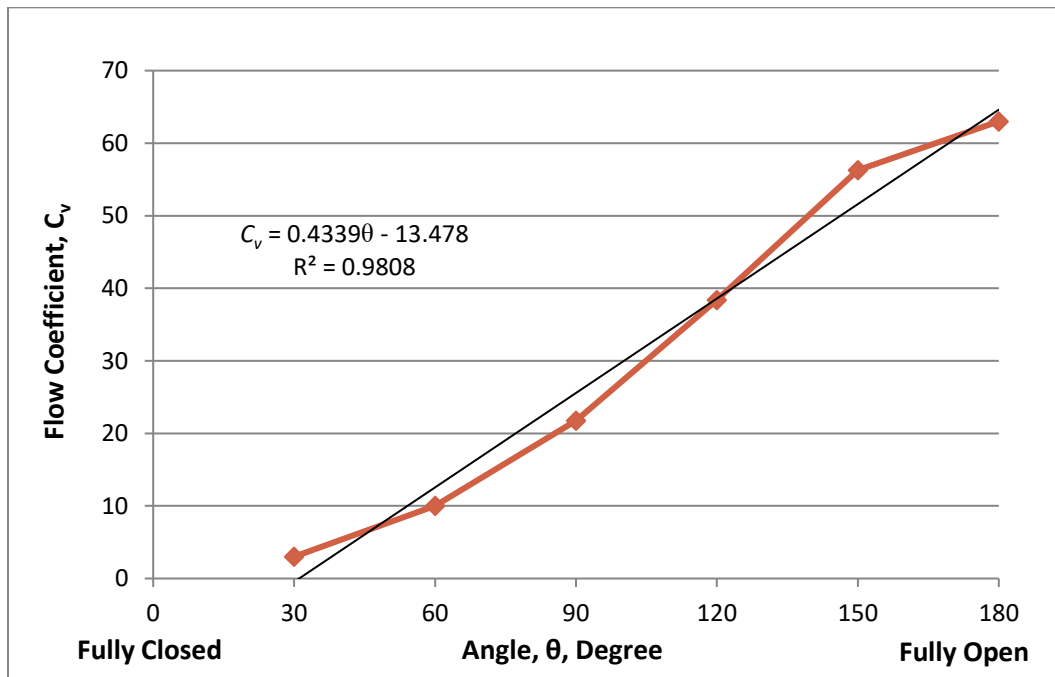


*Figure 4.14: Flow Coefficient vs. Degree of Opening (2<sup>nd</sup> Ball Design)*

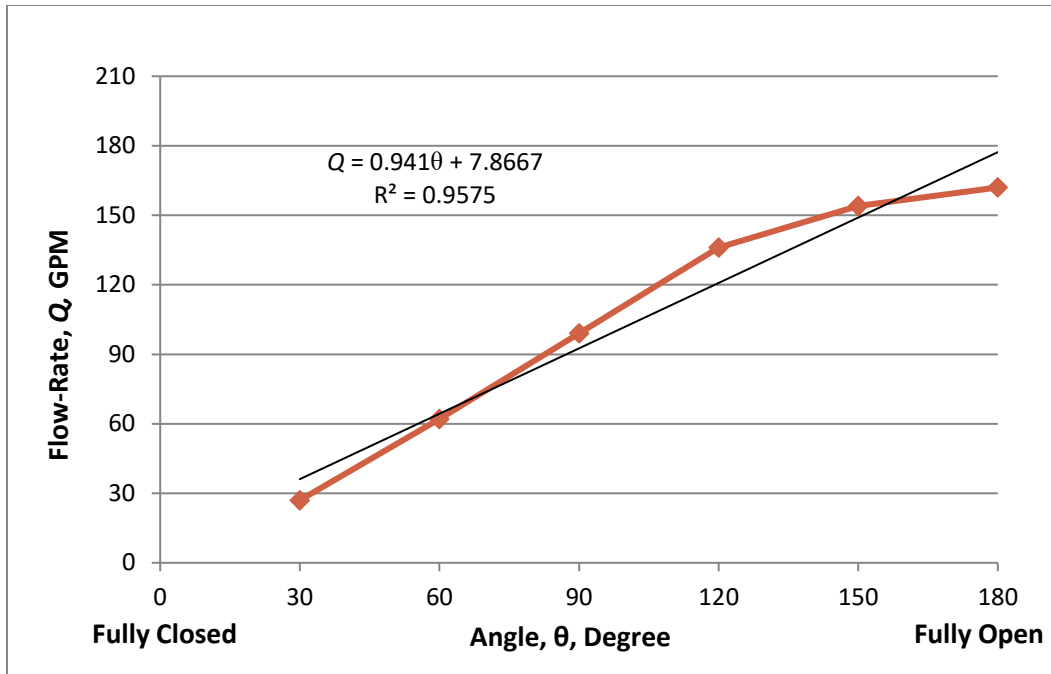


Figure 4.15: Flow-Rate vs. Degree of Opening (2<sup>nd</sup> Ball Design)

Like the CFD model developed for the standard ball and first ball design iteration, the computational simulations for the second ball design iteration tend to predict flow coefficient most accurately in flows that exhibit relatively less turbulence.

Again, the cavitation index of the second ball design is at its highest at the degree of opening nearest the fully closed position. This can be seen in figure 4.16. However, the percent difference values are inconsistent throughout the various degree of opening positions. The presence of cavitation at positions near the fully closed position certainly contributes to discrepancies between experimental and computational flow coefficients. However, cavitation is not the only contributing factor to these discrepancies.

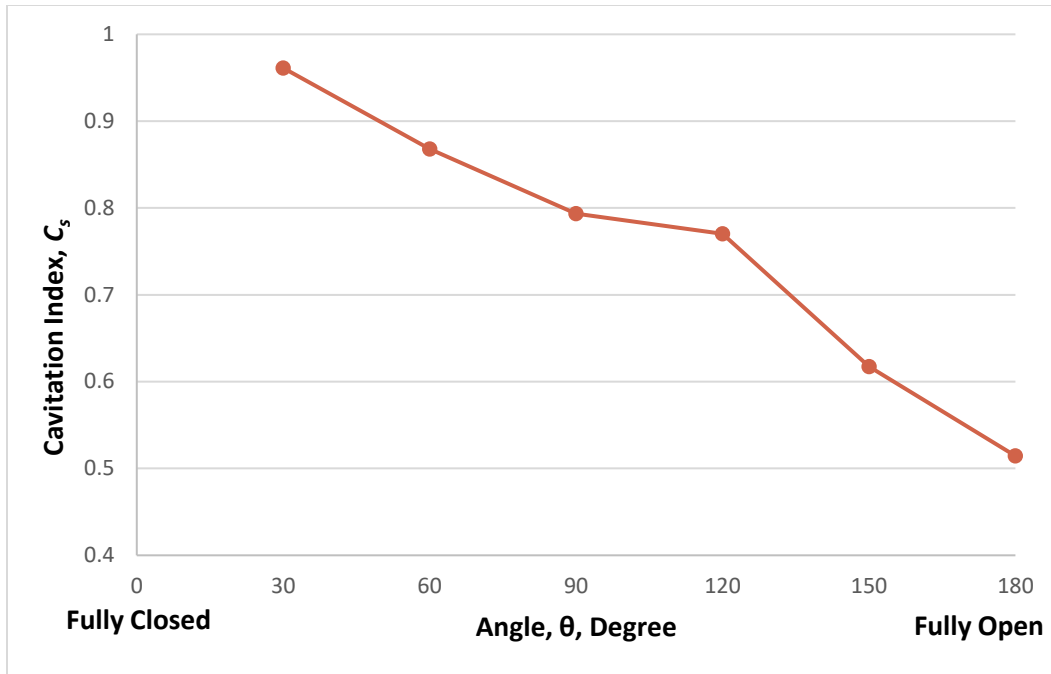


Figure 4.16: Cavitation Index vs. Degree of Opening (2<sup>nd</sup> Ball Design)

In section 4.11 it was mentioned that each 3D model that represented the fluid domain had to omit small volumes to create a mesh of good quality. The fluid domain of the second ball design had to be simplified from its exact representation by the greatest amount. This is due to the sharp angles and thin wall sections found in the second ball design that would cause the FLUENT mesher to create degenerate cells.

#### 4.1.7.4 Comparison of Three Ball Designs

A comparison of the computational results of each ball design can be seen in the following section. Figure 4.17 below illustrates the flow coefficient curves for each design. To quantify how well each ball design's curve fits a linear regression line, a coefficient of determination is calculated from the computational data points. A coefficient of determination, commonly denoted as  $R^2$ , is a statistical measure of how close data points are to the fitted regression line. In figure 4.18 the  $R^2$  values, with regards to computational flow coefficients, can be seen.

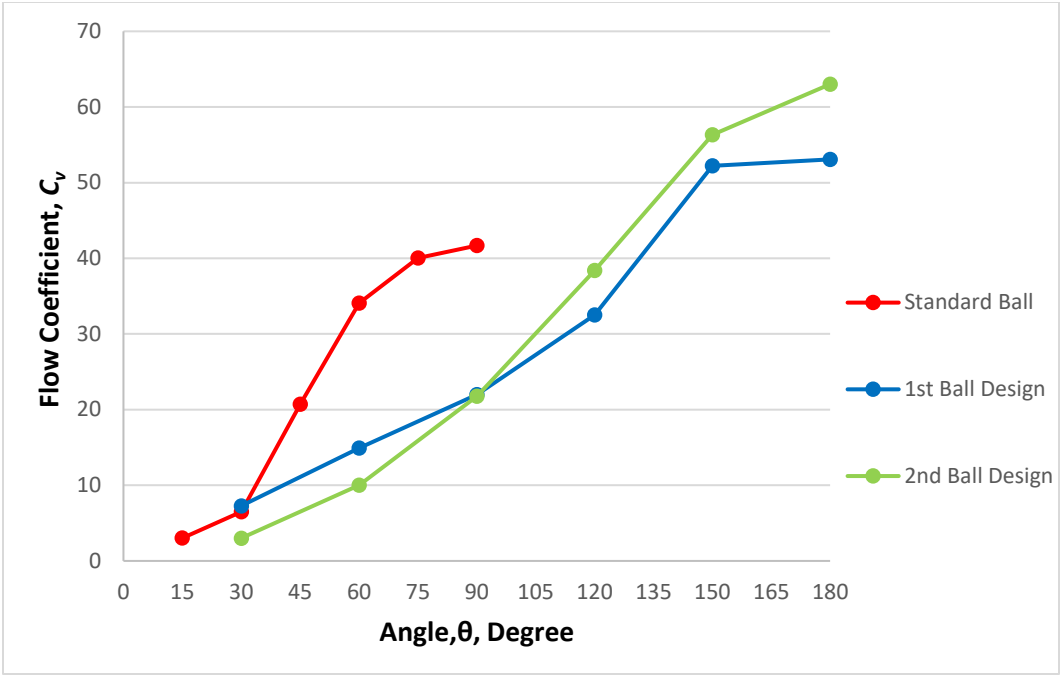


Figure 4.17: Comparison of Computational Flow Coefficient Curves

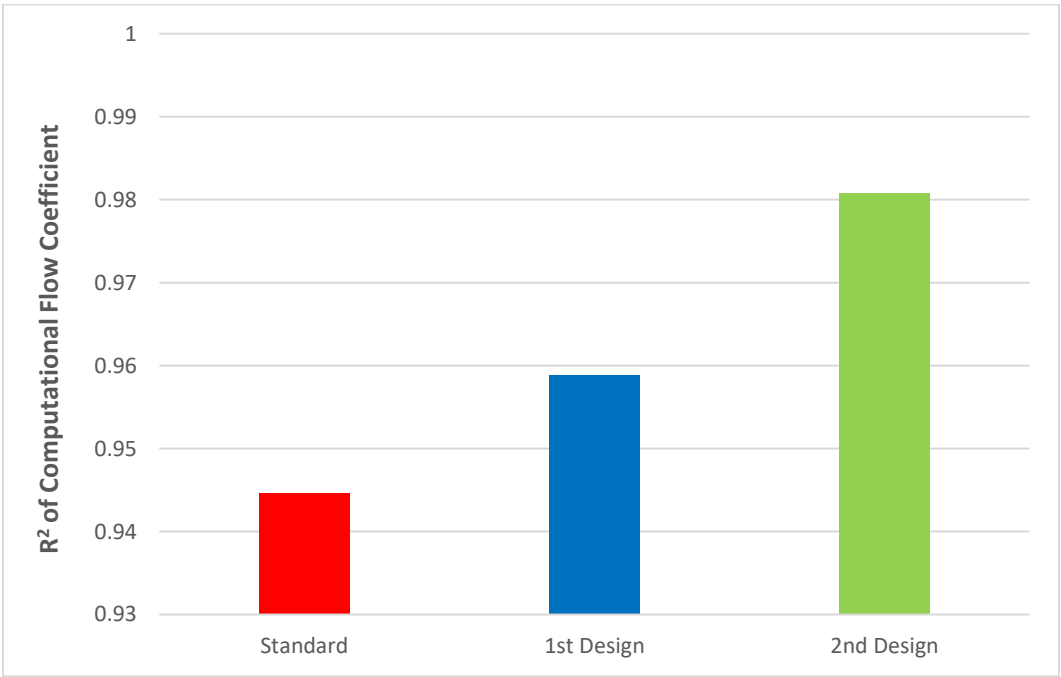
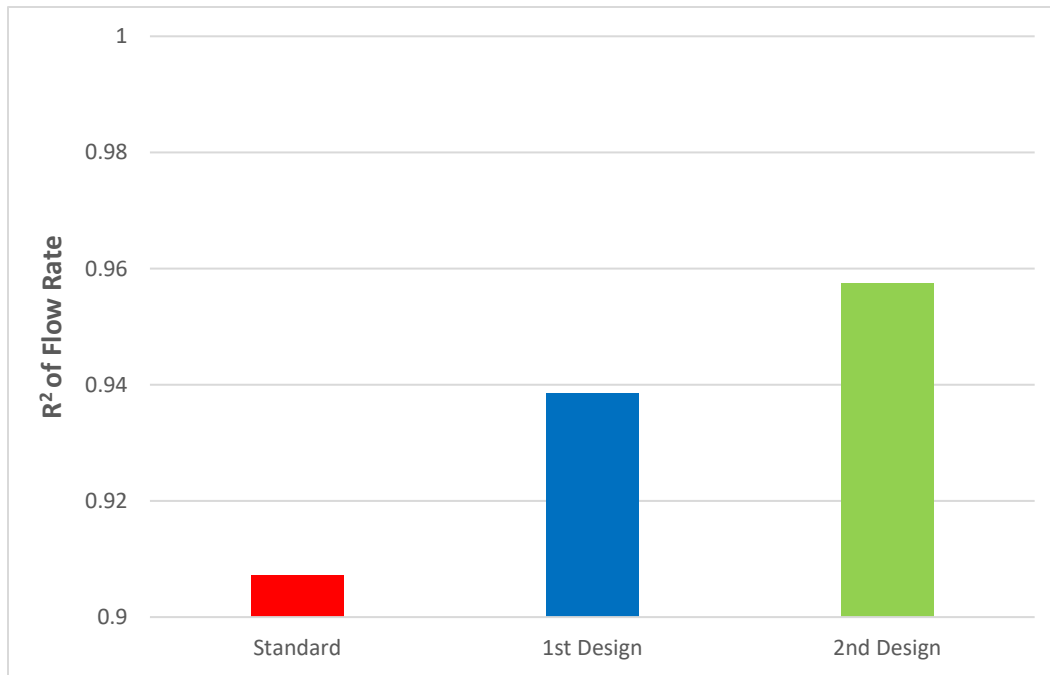


Figure 4.18: Computational  $R^2$  Comparison of Three Ball Designs (Flow Coefficient)

Based on the  $R^2$  values in figure 4.18, the CFD model developed in this study demonstrates that the second ball design has the most linear relationship between flow

coefficient and degree of opening. The CFD models also show that the second ball design has the most linear relationship between volumetric flow-rate and degree of opening. This claim is supported by the  $R^2$  values shown in figure 4.19 below. In figure 4.19 the  $R^2$  values clearly show that the flow rate curve for the second ball design is the most linear among the three designs.



*Figure 4.19: Computational  $R^2$  Comparison of Three Ball Designs (Flow-Rate)*

## 4.2 Physical Experimentation

The following sections will describe the experimental procedure, the experimental results, and potential sources of error.

### 4.2.1 Purpose

The purpose of conducting physical experimentation was to analyze the capability of a CFD model to accurately capture physical phenomena. To accomplish this each of the three ball designs in this study were manufactured to collect physical data. Results of physical experimentation were then compared to computational results.

#### 4.2.2 Test Specimen

The test specimen in this study were three unique bottom-load balls. Each design features a 1.5-inch diameter inlet and outlet. Of the three designs, the standard ball is manufactured from 316 stainless steel and has the finest surface finish. The other two ball designs, first ball design and second ball design, are fabricated through additive manufacturing and are made of ABS plastic. The first ball design and second ball design have a much rougher surface finish than the standard ball. Images of each design can be seen in chapter one, in figure 1.3.

The standard ball differs from the other two designs in that it rotates from its fully closed to fully open position in a  $90^\circ$  turn. Both the first and second ball designs take approximately  $180^\circ$  to travel from fully closed to the fully open position. The first and second ball designs feature an outside groove that gradually increases as the ball is rotated from its fully closed to fully open positions.

#### 4.2.3 Equipment

To capture physical data, several measurement devices and tools were used. In figure 4.20 below one can see a schematic of the simple circuit that was constructed to test each ball design and where each measurement device and tool is located.

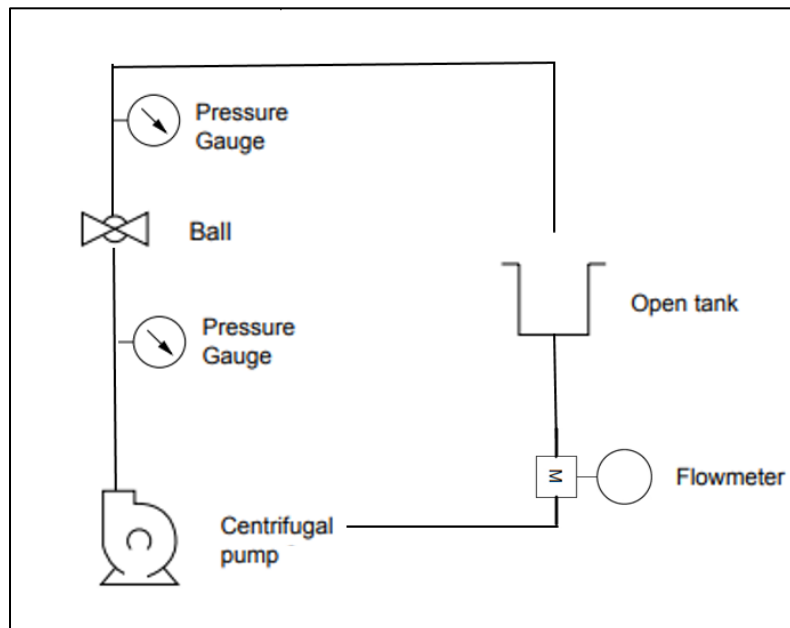
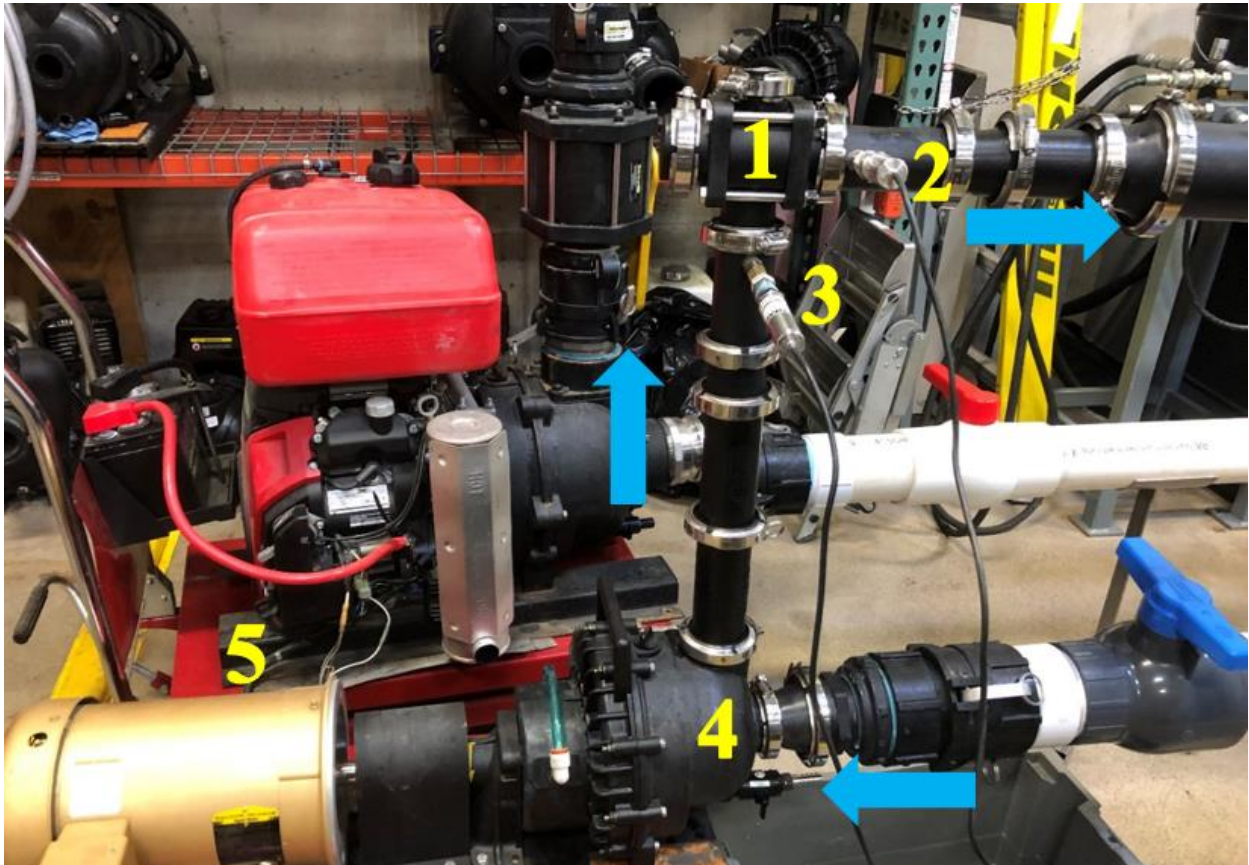


Figure 4.20: Test Circuit Schematic

In figure 4.21 below, part of the physical circuit can be seen. Each measurement device and component, apart from the magnetic flowmeter and open tank, is labeled. The direction of flow is called out in blue markers. The magnetic flow meter is located upstream of the centrifugal pump. The line downstream of the bottom-load ball valve returns fluid to the open tank.



*Figure 4.21: Physical Test Circuit*

Test Circuit Components:

1. 2" Bottom-load Ball Valve
2. Pressure Transducer at outlet
3. Pressure Transducer at inlet
4. 2" Full Port Centrifugal Pump
5. Electric Motor

Detailed images of the two primary measurement devices, the pressure transducers and magnetic flow meter, can be seen in figures 4.22 – 4.23. The pressure transducers are manufactured by Omega Engineering. The magnetic flowmeter is manufactured by Seametrics. Each measurement device's full specifications can be found in section 4.2.6.



*Figure 4.22: Omega Pressure Transducer*



*Figure 4.23: Magnetic Flowmeter*

To measure the degree of opening for each ball design, a simple angle indicator was 3D printed to fit over the bottom-load ball valve housing. The indicator had a resolution of  $5^\circ$  and a range of  $0^\circ - 180^\circ$ . An image of this indicator can be seen below in figure 4.24.

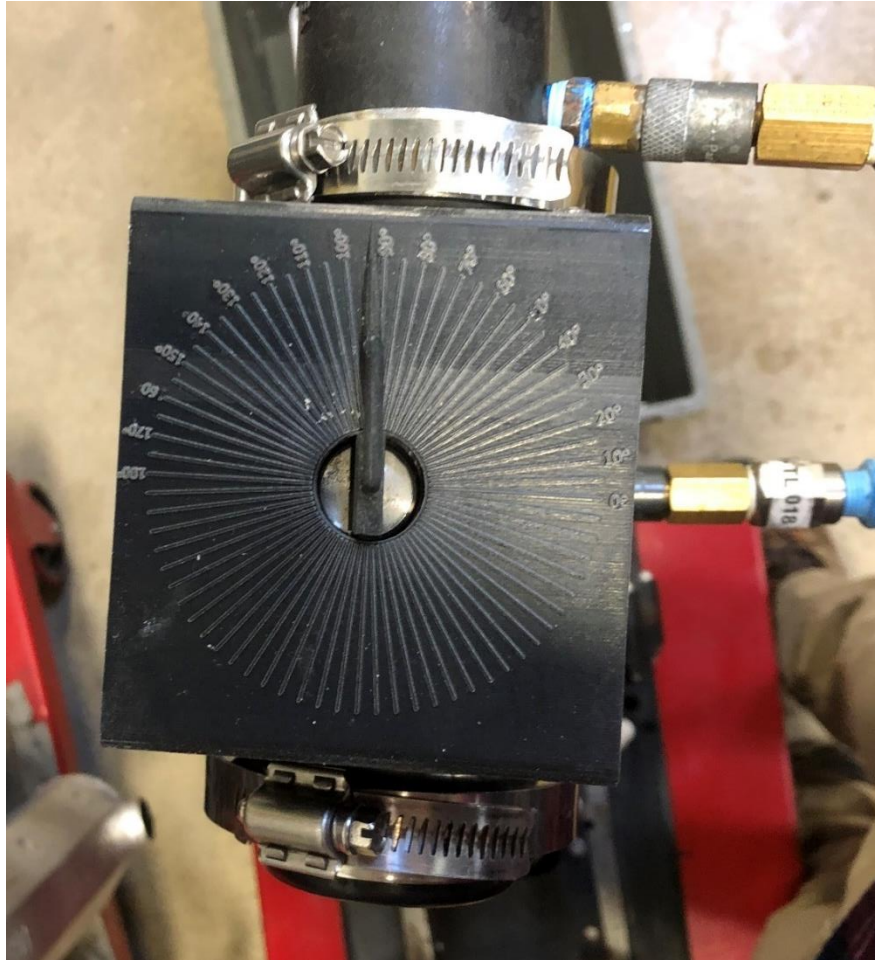


*Figure 4.24: Angle Indicator*

#### 4.2.4 Testing Procedure

The testing procedure began by placing the bottom-load ball valve into the testing circuit shown in figure 4.21. The electric motor was then started and began powering the centrifugal pump. The pump was run continuously for approximately 60 seconds or until a steady output was reached on the flowmeter's digital readout. A single value for flow rate was recorded in U.S. gallons per minute (GPM) once it was observed that the flowmeter's output was steady. At this

point in the testing procedure, values for pressure were recorded in pounds per square inch (PSI) from each pressure transducer. Each pressure transducer's output was displayed on a laptop.

Once flow rate and pressure across the valve had been recorded for a given degree of opening, the valve's ball was rotated to the next position of interest. This testing procedure was repeated for six unique degrees of opening, which are identical to the positions studied in the computational analysis. Once testing for one ball design was completed, the bottom-load ball valve was removed from the testing circuit. The ball valve was then dismantled and the regulating ball inside was replaced with the next design to be tested. This was repeated for all designs. The bottom-load ball valve was then re-inserted into the testing circuit to continue the testing procedure.

#### 4.2.5 Experimental Results

##### 4.2.5.1 Standard Ball Design

The experimental results for the standard ball design agree with the computational results that it does not exhibit a linear relationship between flow coefficient and degree of opening. The data collected from the testing procedure can be seen in table 4.7. The experimental flow coefficient curve can be seen below in figure 4.25.

*Table 4.7: Experimental Test Data (Standard Ball)*

Degree of Opening	Pressure In (PSI)	Pressure Out (PSI)	Pressure Drop (PSI)	Flow-rate (GPM)	Flow Coefficient, $C_v$
90°	10	-4.1	14.1	155	41.28
75°	10.2	-4.4	14.6	149	39.00
60°	15.5	-4.8	20.3	139	30.85
45°	27.6	-6.6	34.2	109	18.64
30°	40.2	-7.6	47.8	53.1	7.68
15°	44.9	-3.2	48.1	20.2	2.91

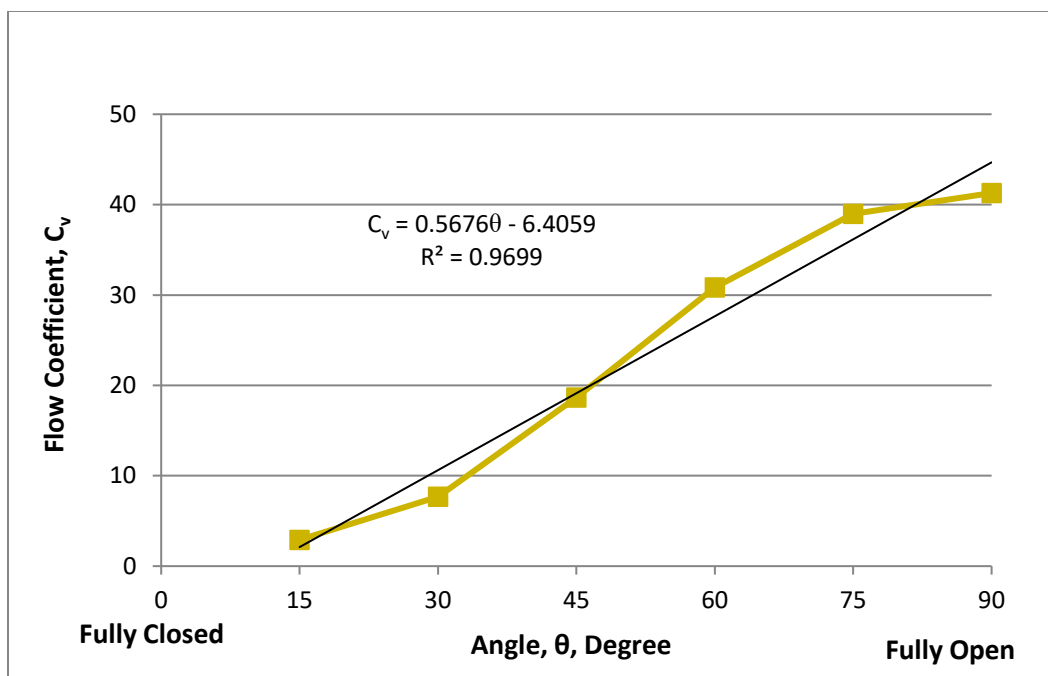


Figure 4.25: Experimental Flow Coefficient vs. Degree of Opening (Standard Ball)

The experimental flow rate versus degree of opening curve is identical to the computational curve shown in figure 4.9. This is because the boundary condition of velocity at the inlet was based on experimental tests. Experimental and computational flow rate curves are identical for each design.

#### 4.2.5.2 First Ball Design

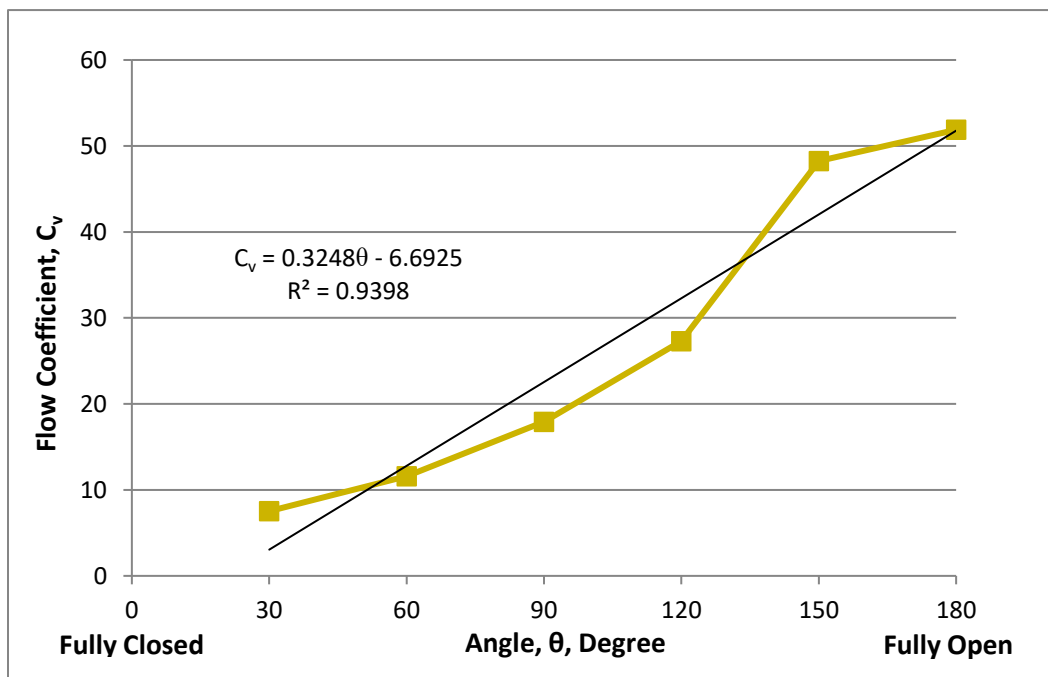
The experimental results for the first ball design agree with the computational results that it does not exhibit a linear relationship between flow coefficient and degree of opening. The data collected from the testing procedure can be seen in table 4.8. The experimental flow coefficient curve can be seen below in figure 4.26.

Table 4.8: Experimental Test Data (First Ball Design)

Degree of Opening	Pressure In (PSI)	Pressure Out (PSI)	Pressure Drop (PSI)	Flow-rate (GPM)	Flow Coefficient, $C_v$
180°	4.85	-4.9	9.75	162	51.88
150°	6.01	-4.71	10.72	158	48.26
120°	24.14	-5.28	29.42	148	27.29

Table 4.8 (continued)

90°	28.45	-5.2	33.65	104	17.93
60°	36.5	-7.5	44	77	11.61
30°	39.8	-6.1	45.9	51	7.53

Figure 4.26: Experimental Flow Coefficient vs. Degree of Opening (1<sup>st</sup> Ball Design)

#### 4.2.5.3 Second Ball Design

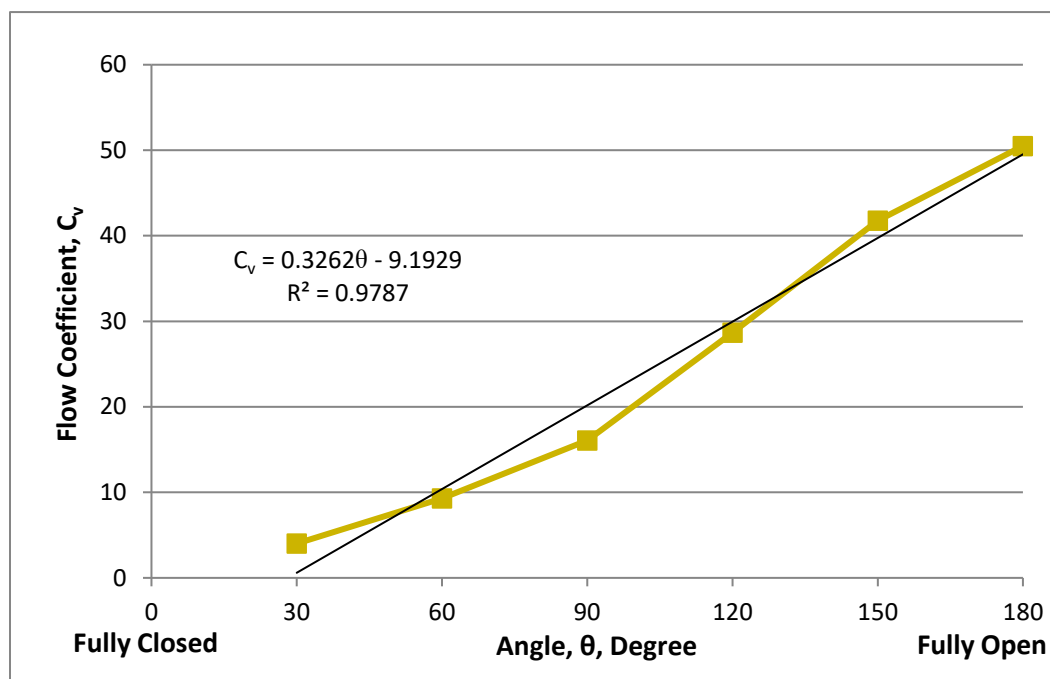
The experimental results for the first ball design agree with the computational results that it does exhibit a linear relationship between flow coefficient and degree of opening. The data collected from the testing procedure can be seen in table 4.9. The experimental flow coefficient curve can be seen below in figure 4.27.

Table 4.9: Experimental Test Data (2<sup>nd</sup> Ball Design)

Degree of Opening	Pressure In (PSI)	Pressure Out (PSI)	Pressure Drop (PSI)	Flow-rate (GPM)	Flow Coefficient
180	5.55	-4.74	10.29	162	50.50
150	8.64	-4.94	13.58	154	41.79
120	17.56	-4.9	22.46	136	28.70

Table 4.9: (continued)

90	30.43	-7.6	38.03	99	16.05
60	38.75	-5.6	44.35	62	9.31
30	43.8	-1.5	45.3	27	4.01

Figure 4.27: Experimental Flow Coefficient vs Degree of Opening (2<sup>nd</sup> Ball Design)

#### 4.2.5.4 Comparison of Three Ball Designs

A comparison of the experimental results of each ball design can be seen in the following section. Figure 4.28 below illustrates the flow coefficient curves for each design. To quantify how well each ball design's curve fits a linear regression line, a coefficient of determination is calculated from the experimental data points. In figure 4.29 the  $R^2$  values, with regards to experimental flow coefficients, can be seen.

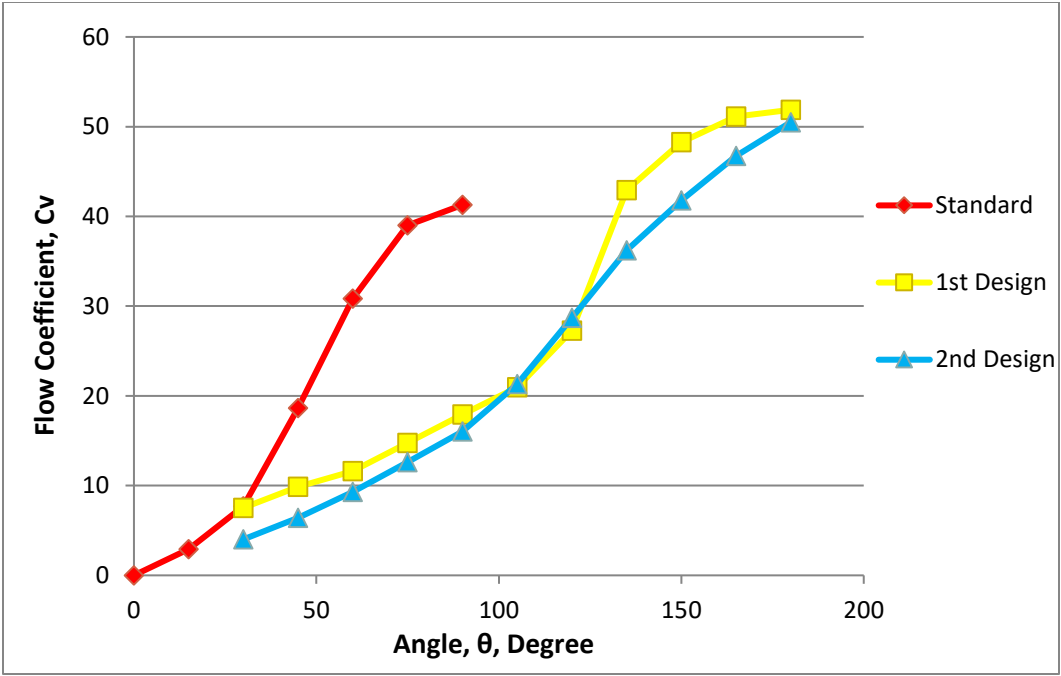


Figure 4.28: Comparison of Experimental Flow Coefficient Curves

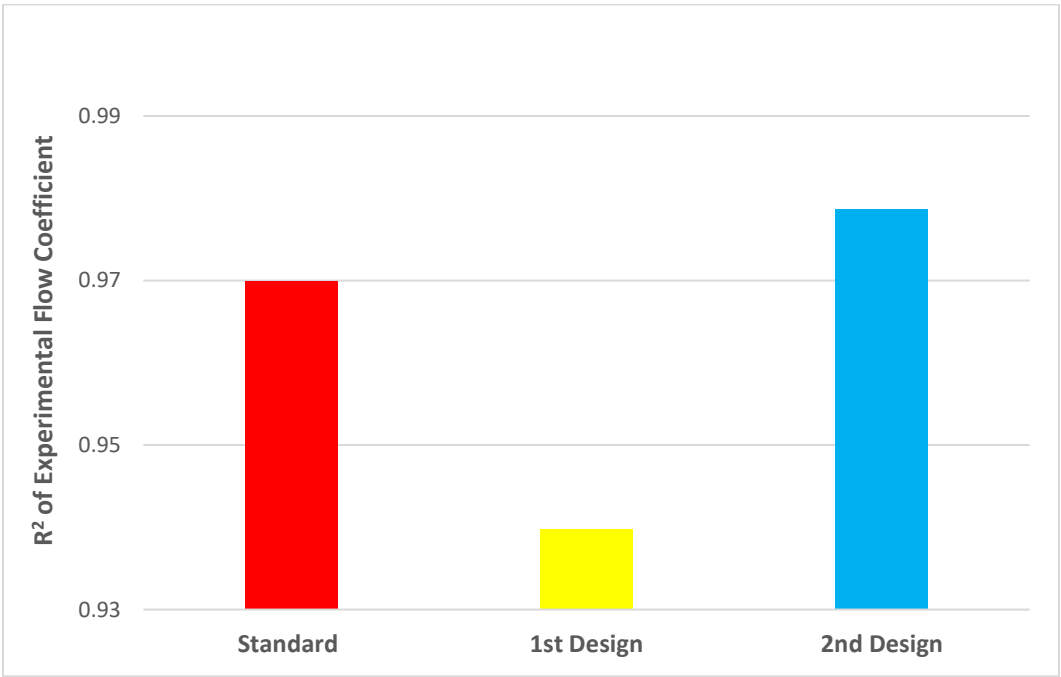


Figure 4.29: Experimental R<sup>2</sup> Comparison of Three Designs (Flow Coefficient)

Based on the R<sup>2</sup> values in figure 4.28, the experimental data collected in this study demonstrates that the second ball design has the most linear relationship between flow

coefficient and degree of opening. The experimental data also show that the second ball design has the most linear relationship between volumetric flow-rate and degree of opening. This claim is supported by the  $R^2$  values shown in figure 4.19. The  $R^2$  values for computational flow rate and experimental flow rate are identical because the boundary condition of velocity at the inlet was found using experimental data. In figure 4.19 the  $R^2$  values clearly show that the flow rate curve for the second ball design is the most linear among the three designs.

#### 4.2.6 Sources of Error

Error in the experimental procedure affected the measurement of three parameters. The first parameter was the degree of opening. Degree of opening was measured using a 3D printed angle indicator as shown in figure 4.24. This measurement was highly susceptible to human error because the measurement relied on a tester's visual perception. There are also clearances and allowances between the valve stem and ball in a valve. These clearances allow the stem to rotate slightly before rotating the ball in the valve.

The other two parameters were pressure and flow rate. Error in these parameters can be quantified. The Omega pressure transducers used in this study claim a full-scale error of  $\pm 0.5\%$ . The Seametrics magnetic flowmeter claims a full-scale error  $\pm 0.75\%$ . The full specifications of both the Omega pressure transducers and Seametrics magnetic flowmeter can be found in the Appendix. Total error was quantified by equation (14) below.

$$Total\ Error = \sqrt{e_1^2 + e_2^2 + \dots + e_n^2} \quad (14)$$

Total error is approximately 1% based on the stated accuracy of the measurement devices used this study. There are other sources of error present in this study, however, the magnitudes of these errors were not quantified in this study. These unquantified sources of error are mechanical vibration and electrical noise.

### 4.3 Comparison of Experimental and Computational Results

#### 4.3.1 Comparison of Flow Coefficient Curves

In this section a comparison of the flow coefficient curves from the experimental and computational methods can be seen. The second ball had the highest percent difference between computational and experimental results of the three designs that were analyzed in this study. Potential explanations for this discrepancy can be found in section 4.1.7.3. Percent difference between experimental and computational methods was lowest at the fully open positions that exhibit relatively uninterrupted flows. This observation was common among all three ball designs. Percent difference grew as the degree of opening decreased. The degree of openings closest to the fully closed position reversed this trend in all three designs. This may be due to the presence of cavitation. Comparisons of computational and experimental results for each design can be seen below in figures 4.30 - 4.32.

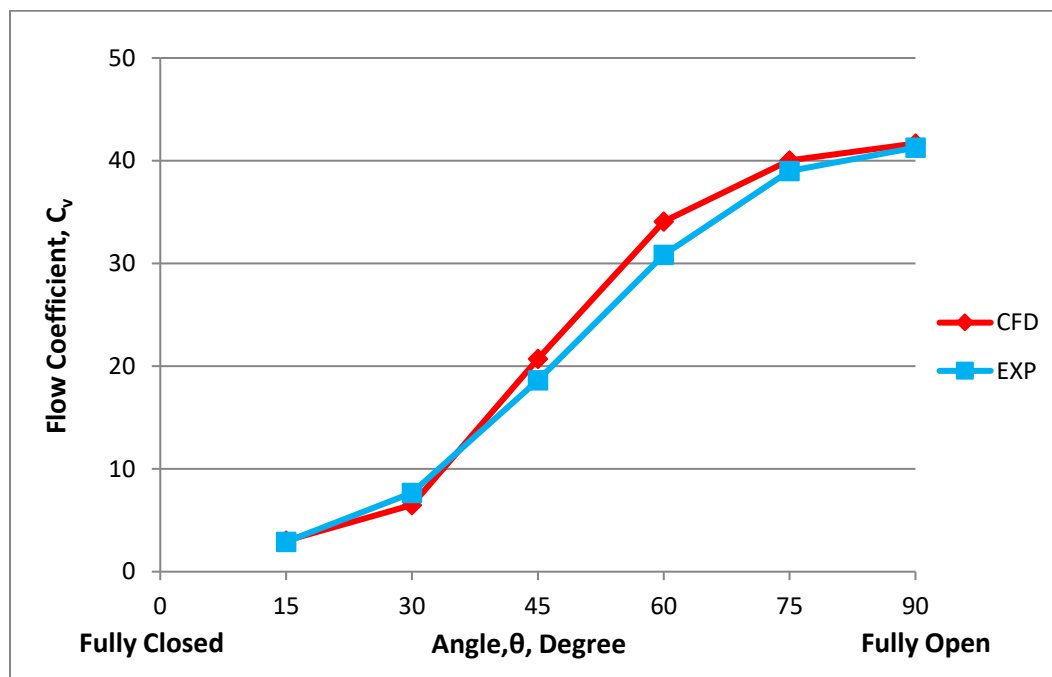


Figure 4.30: Comparison of Flow Coefficient Curves (Standard Ball)

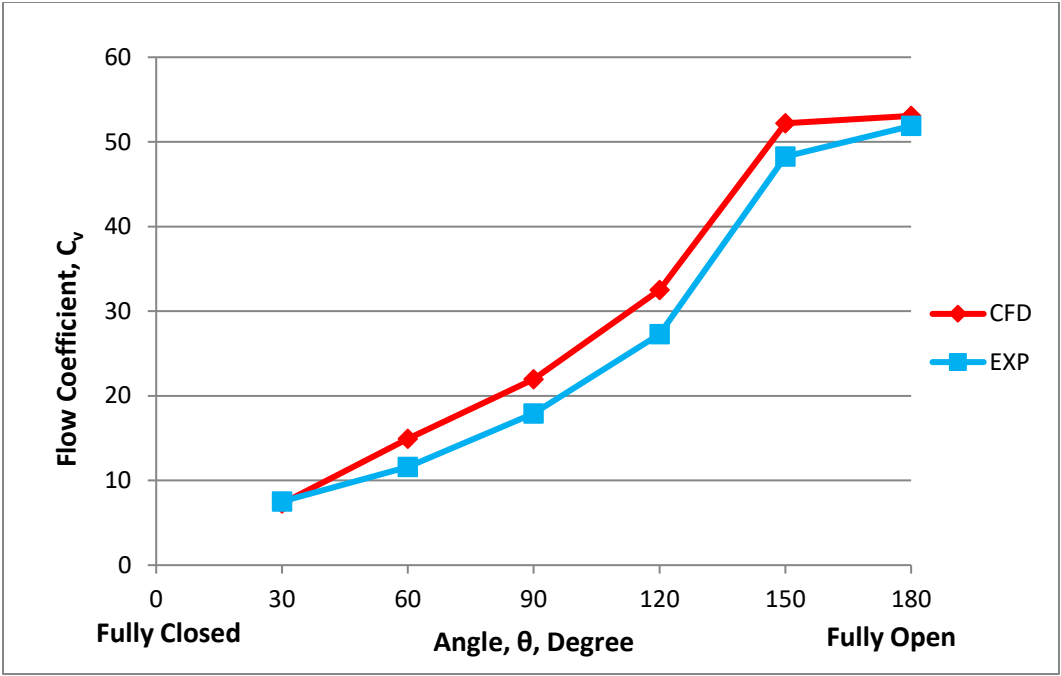


Figure 4.31: Comparison of Flow Coefficient Curves (1<sup>st</sup> Ball Design)

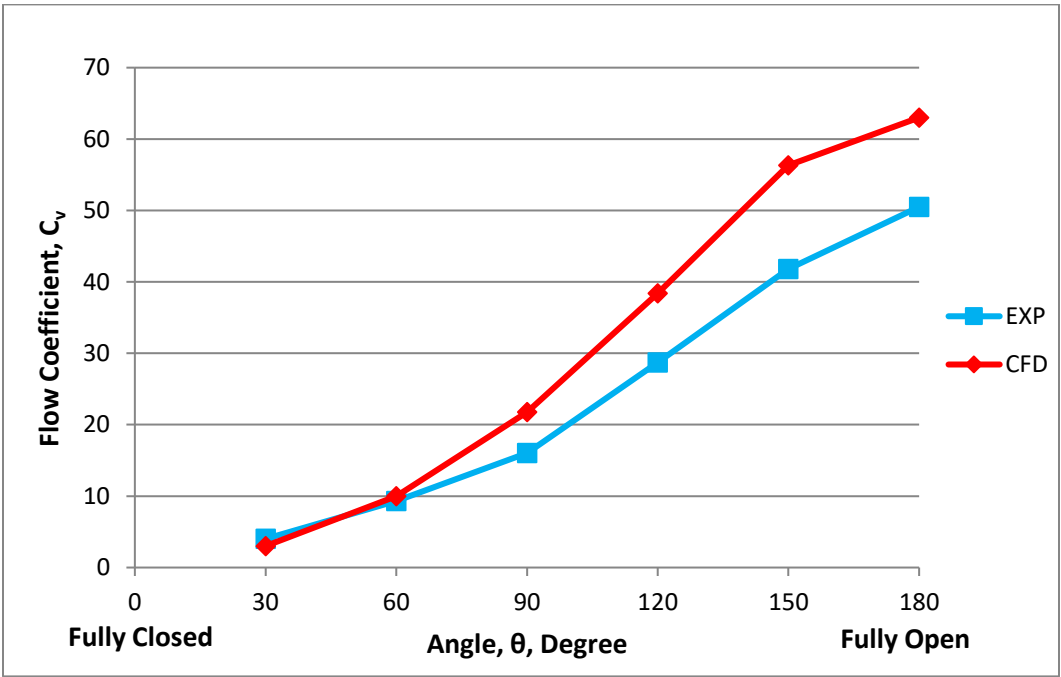
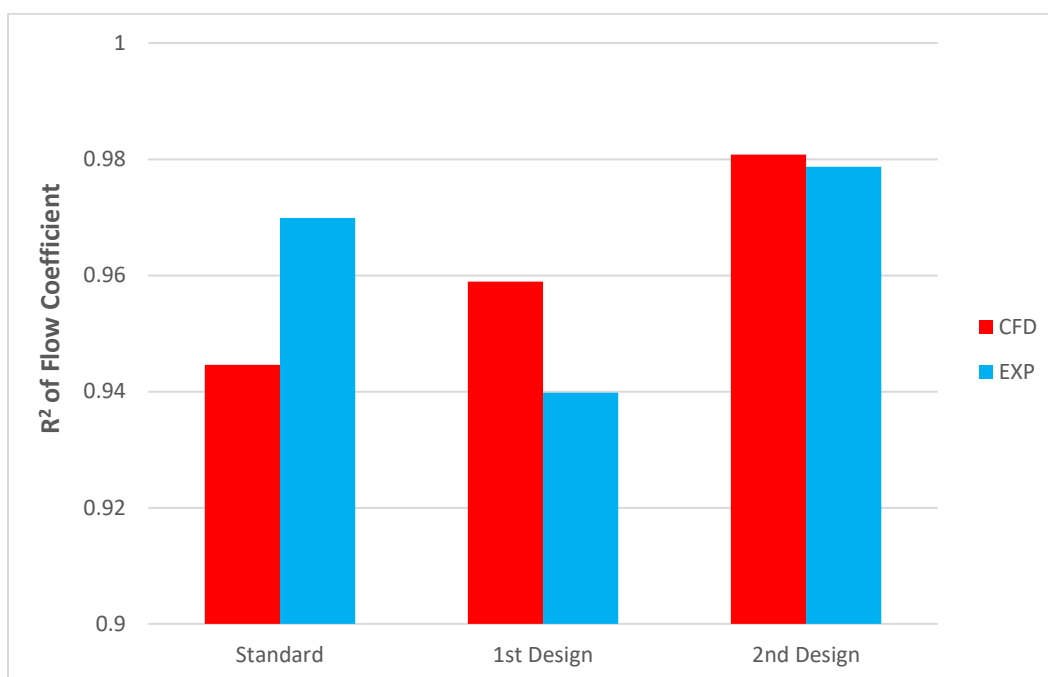


Figure 4.32: Comparison of Flow Coefficient Curves (2<sup>nd</sup> Ball Design)

### 4.3.2 Comparison of $R^2$ Values

As mentioned previously, the flow rate curves for both computational and experimental methods are identical. This is because the boundary condition of velocity at the inlet was determined from experimental flow rates. Therefore, the  $R^2$  values for flow rate between the experimental and computational methods will be identical.

However, the  $R^2$  values for flow coefficient are not identical. This is because the computational models calculate pressure drop across the fluid domain based on a variety of parameters including, mesh quality and size, turbulence model, boundary conditions, fluid properties, etc. In figure 4.33 below one can see the comparison of the  $R^2$  values for each ball design and analysis method (computational or experimental).



*Figure 4.33:  $R^2$  Comparison of Computational and Experimental Methods*

As can be seen in figure 4.33, both the computational and experimental method show that the second ball design most closely fits a linear regression line. However, the computational model does not agree with experimental data for the first ball design. The computational model shows that the first ball design exhibits a more linear flow coefficient curve than the standard

ball, but the experimental data refutes this claim. Potential explanations for this discrepancy can be found in sections 4.17 and 4.26.

Based on figures 4.30 – 4.32, percent difference between computational and experimental flow coefficients are largest for the second ball design. As previously discussed, one contributing source of error is the higher turbulence observed in the second ball design. The turbulence formed at the fully open position for the second ball design can be seen in figure 4.34.

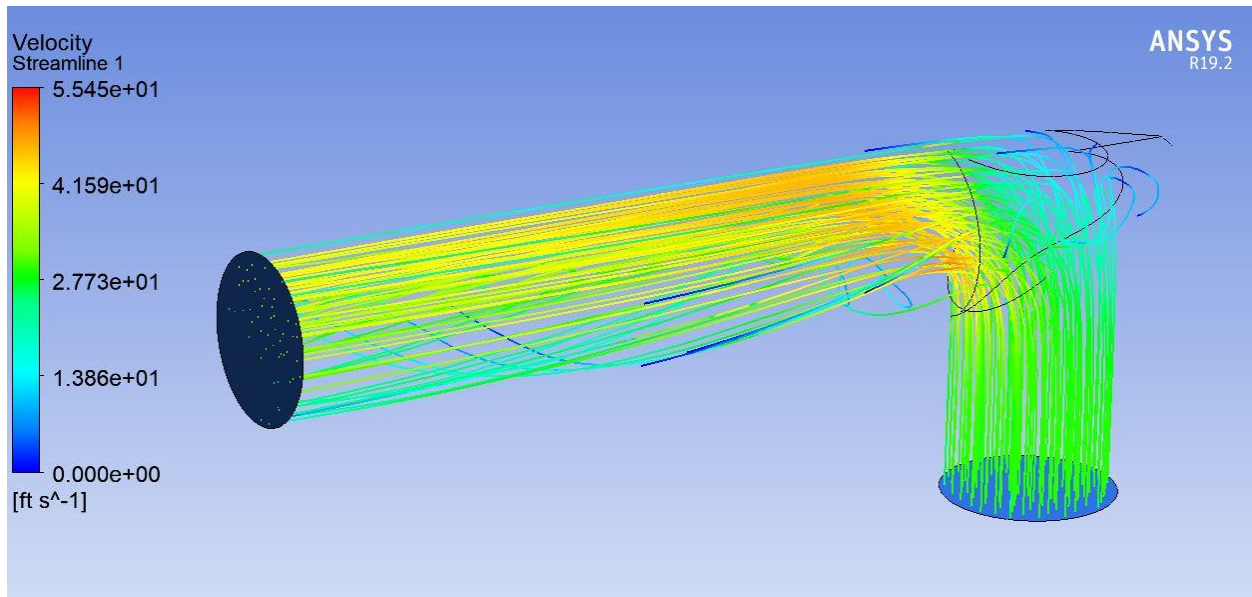


*Figure 4.34: Flow Streamlines of 2<sup>nd</sup> Ball Design*

For the same degree of opening figures 4.35 – 4.36 clearly demonstrate that the second ball design has a higher turbulent kinetic energy than the first ball design.

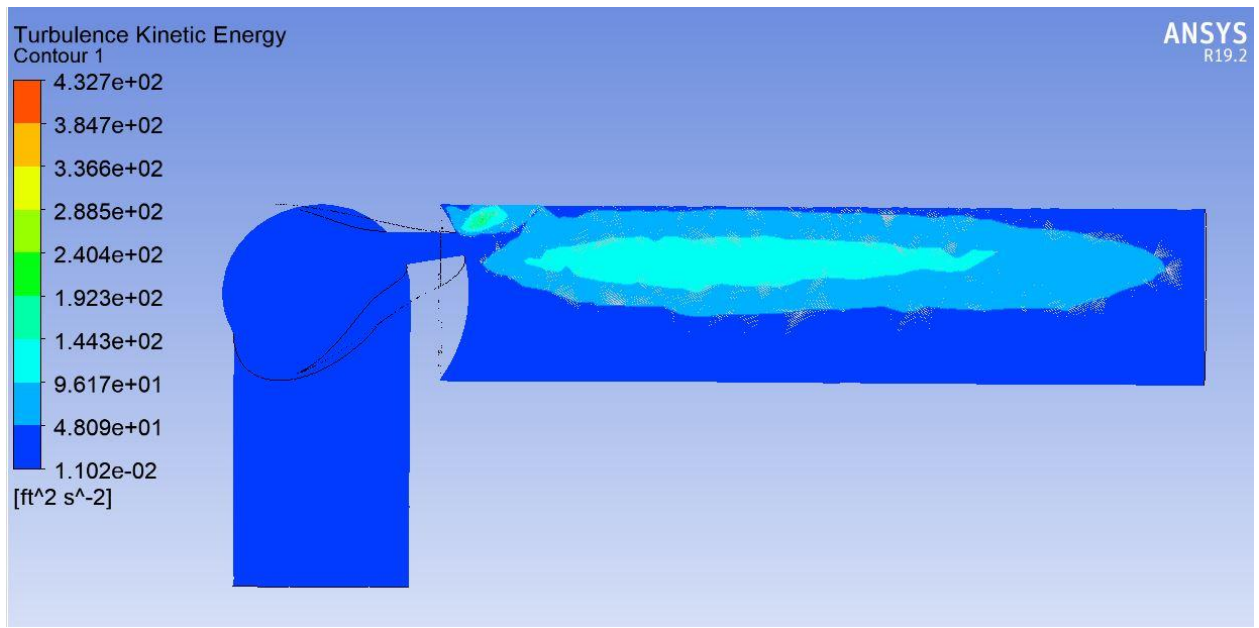


Figure 4.35: Turbulent Kinetic Energy (2<sup>nd</sup> Ball Design)

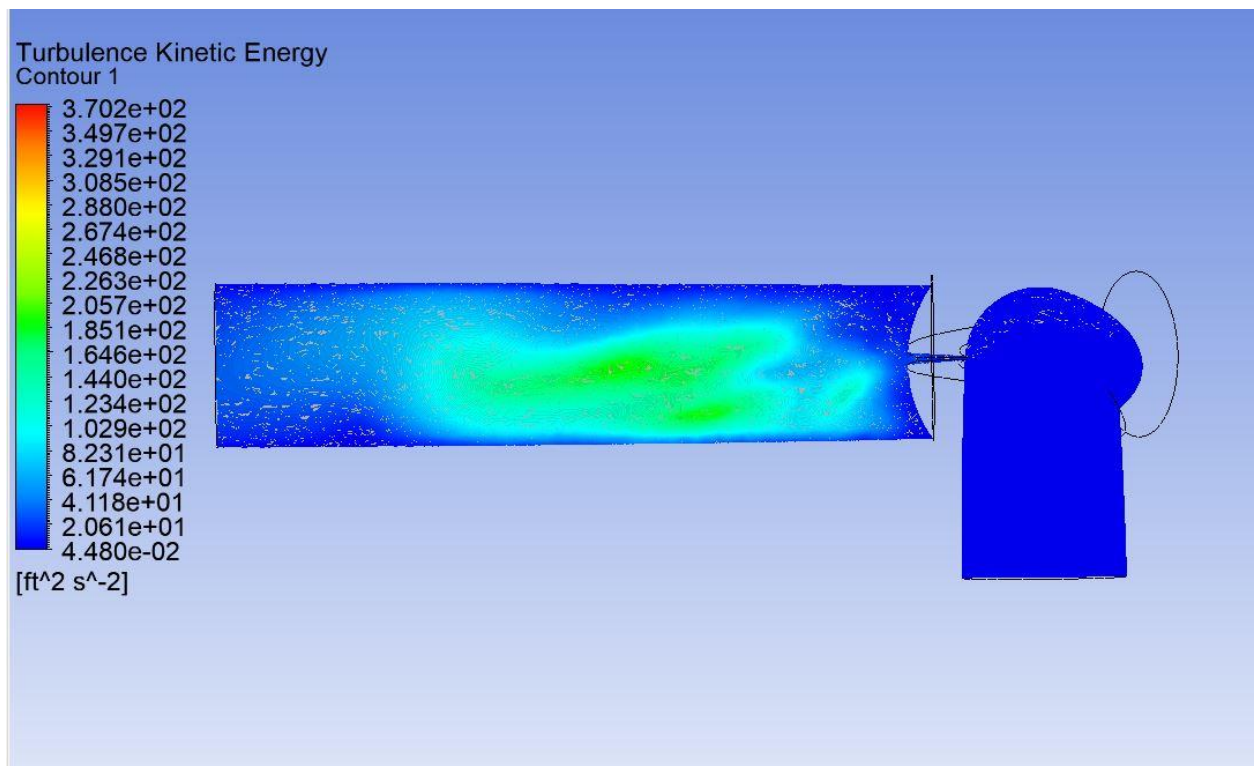


Figure 4.36: Turbulent Kinetic Energy (1<sup>st</sup> Ball Design)

## CHAPTER 5. SUMMARY, CONCLUSIONS, and RECOMMENDATIONS

### 5.1 Summary

This study analyzed the capability of a CFD model to predict the characteristics of three ball designs for flow regulating purposes. The primary characteristic that was analyzed was the flow coefficient of each design at various positions.

A CFD model's capability to accurately predict flow coefficient was based on a comparison to experimental data. To capture experimental data, a simple test circuit was constructed. Each of the three ball designs were manufactured and tested in this circuit. The standard ball design is a production part and was readily available in 316 stainless steel with a fine surface finish. The first and second ball designs were created through additive manufacturing and made of ABS plastic.

A comparison of data from the computational and experimental methods show that a CFD model can predict flow coefficient to varying levels of accuracy. One of the primary factors that influence the accuracy of a CFD model is the turbulence model chosen to simulate turbulence created by the fluid domain. As turbulence created in experimental tests grow more complex, the turbulence model will have an increasing amount of deviation from experimental data.

Another factor that affects a CFD model's accuracy is the representation of the fluid domain. In this study the fluid domain had to be simplified for each ball design. The second design was simplified by the greatest amount. This was done to reduce the number of degenerate cells in a mesh.

The possibility of cavitation forming at low degrees of opening is another factor that affects a CFD model. In this study a single phase CFD model was used for all computational analyses. To accurately model the effects of cavitation, a multi-phase CFD model must be used.

The computational and experimental methods agree that modifying the design of a traditional bottom-load ball to the second ball design would increase the linearity of its flow coefficient curve with respect to degree of opening.

## 5.2 Conclusions

The conclusion of this study was that a CFD model can generally predict the relationship between flow coefficient and degree of opening for a ball design. Values for flow coefficient were most accurately predicted at the fully open positions of each ball design. Percent difference between computational and experimental data for flow coefficient was at its lowest at the fully open position. The average percent difference between computational and experimental methods was 9.35% at the fully open position.

Percent difference between methods was observed to grow as the degree of opening decreased. This may be due to a variety of factors including representation of the fluid domain, mesh quality, turbulence model, and cavitation.

This study found that the modifications found in the second ball design increase linearity of flow coefficient by the greatest amount. This study also found that the modifications found in the second ball design increase linearity of flow rate by the greatest amount. This claim is supported by both computational and experimental data.

## 5.3 Recommendations

This study recommends that an investigation into cavitation at low degrees of opening be conducted to observe if cavitation is occurring. This study also recommends that a transient computational model be studied to observe if any output parameters such as pressure drop fluctuate over time. Future studies should also investigate the use of other turbulence models. It is also recommended that ball designs be manufactured from the same material to eliminate any discrepancies between surface roughness or Reynolds number. The final recommendation is that future studies investigate the use of various meshing techniques to more accurately represent the fluid domain of each ball design without creating degenerate cells.

## LIST OF REFERENCES

- Cai, J., Braun, J. E., Laboratories, R. W. H., & Lafayette, W. (2016). Self-Learning Backlash Inverse Control of Cooling or Heating Coil Valves Having Backlash Hysteresis \* Corresponding Author. *International Compressor Engineering, Refrigeration and Air Conditioning, and High Performance Buildings Conferences*, 1–11.
- Chern, M.-J., & Wang, C.-C. (2004). Control of Volumetric Flow-Rate of Ball Valve Using V-Port. *Journal of Fluids Engineering*, 126(3), 471. <https://doi.org/10.1115/1.1760536>
- Durran, D. R. (1989). Improving the Anelastic Approximation. *Journal of the Atmospheric Sciences*, 46(11), 1453–1461. [https://doi.org/10.1175/1520-0469\(1989\)046<1453:ITAA>2.0.CO;2](https://doi.org/10.1175/1520-0469(1989)046<1453:ITAA>2.0.CO;2)
- Ghoreyshi, M., Bergeron, K., Seidel, J., Lofthouse, A. J., & Cummings, R. M. (2015). Grid Quality and Resolution Effects for Aerodynamic Modeling of Ram-Air Parachutes. *Journal of Aircraft*. <https://doi.org/10.2514/1.c033391>
- Hoffman, J., & Johnson, C. (2007). Computational Turbulent Incompressible Flow. *October*, 4, 415. <https://doi.org/10.1007/978-3-540-46533-1>
- Hutton, D. V. (2004). Fundamentals of Finite Element Analysis. *Textbook (Important)*. <https://doi.org/10.1017/CBO9781107415324.004>
- Menter, F. R., Langtry, R., Völker, S., & Huang, P. G. (2005). Transition Modelling for General Purpose CFD Codes. In *Engineering Turbulence Modelling and Experiments 6*. <https://doi.org/10.1016/B978-008044544-1/50003-0>
- Moujaes, S. F., & Jagan, R. (2008). 3D CFD Predictions and Experimental Comparisons of Pressure Drop in a Ball Valve at Different Partial Openings in Turbulent Flow. *Journal of Energy Engineering*, 134(1), 24–28. [https://doi.org/10.1061/\(ASCE\)0733-9402\(2008\)134:1\(24\)](https://doi.org/10.1061/(ASCE)0733-9402(2008)134:1(24))
- Said, M. M., AbdelMeguid, H. S. S., & Rabie, L. H. (2016). The Accuracy Degree of CFD Turbulence Models for Butterfly Valve Flow Coefficient Prediction. *American Journal of Industrial Engineering*, Vol. 4, 2016, Pages 14-20, 4(1), 14–20. <https://doi.org/10.12691/AJIE-4-1-3>
- Salim, S. M., & Cheah, S. . (2009). □Wall Y+ Strategy for Dealing with Wall-bounded Turbulent Flows. *IMECS 2009*. <https://doi.org/10.1.1.149.722>
- Shih, T.-H., Zhu, J., & Lumley, J. L. (1993). *A Realizable Reynolds Stress Algebraic Equation Model. Nasa Technical Memorandum*.

- Shih, T. H., Zhu, J., & Lumley, J. L. (1995). A new Reynolds stress algebraic equation model. *Computer Methods in Applied Mechanics and Engineering*, 125(1–4), 287–302. [https://doi.org/10.1016/0045-7825\(95\)00796-4](https://doi.org/10.1016/0045-7825(95)00796-4)
- Toro, A. Del. (2012). *Computational Fluid Dynamics Analysis of Butterfly Valve*, Utah State.
- Toro, E. F. (2009). *Riemann solvers and numerical methods for fluid dynamics*. Springer, Berlin. <https://doi.org/10.1007/978-3-540-49834-6>
- Versteeg, H. K., & Malaskeker, W. (2007). *An Introduction to Computational Fluid Dynamics. Fluid flow handbook*. McGraw-Hill ... (Vol. M). <https://doi.org/10.2514/1.22547>
- Wilcox, D. C. (1999). *Turbulence Modeling for CFD*. *Japanese Journal of Applied Physics*.

## APPENDIX

## mV/V OUTPUT HIGH PERFORMANCE PRESSURE TRANSDUCERS PIEZORESISTIVE DESIGN WITH HIGH TEMPERATURE PERFORMANCE

**100 mV Output**  
**0-10 inH<sub>2</sub>O to 0-5000 psi**  
**25 mb to 345 bar**

**PX409 Series**





PX409-100GV,  
shown actual size.



PX419-015GV,  
shown actual size.



PX429-015GV,  
shown actual size.

**Stock Delivery for most Ranges!**

To Order				
RANGE		2 m (6') CABLE	MINI-DIN	TWIST-LOCK
psi	bar	TERMINATION	TERMINATION	TERMINATION
mV/V OUTPUT, GAGE PRESSURE RANGES				
10 in-H <sub>2</sub> O	25 mb	PX409-10WGV	PX419-10WGV	PX429-10WGV
1	69 mb	PX409-001GV	PX419-001GV	PX429-001GV
2.5	172 mb	PX409-2.5GV	PX419-2.5GV	PX429-2.5GV
5	345 mb	PX409-005GV	PX419-005GV	PX429-005GV
15	1.0	PX409-015GV	PX419-015GV	PX429-015GV
30	2.1	PX409-030GV	PX419-030GV	PX429-030GV
50	3.4	PX409-050GV	PX419-050GV	PX429-050GV
100	6.9	PX409-100GV	PX419-100GV	PX429-100GV
150	10.3	PX409-150GV	PX419-150GV	PX429-150GV
250	17.2	PX409-250GV	PX419-250GV	PX429-250GV
500	34.5	PX409-500GV	PX419-500GV	PX429-500GV
750	51.7	PX409-750GV	PX419-750GV	PX429-750GV
1000	69	PX409-1.0KGV	PX419-1.0KGV	PX429-1.0KGV
1500	103	PX409-1.5KGV	PX419-1.5KGV	PX429-1.5KGV
2500	172	PX409-2.5KGV	PX419-2.5KGV	PX429-2.5KGV
3500	241	PX409-3.5KGV	PX419-3.5KGV	PX429-3.5KGV
5000	345	PX409-5.0KGV	PX419-5.0KGV	PX429-5.0KGV
mV OUTPUT, ABSOLUTE PRESSURE RANGES				
5	345 mb	PX409-005AV	PX419-005AV	PX429-005AV
15	1.0	PX409-015AV	PX419-015AV	PX429-015AV
30	2.1	PX409-030AV	PX419-030AV	PX429-030AV
50	3.4	PX409-050AV	PX419-050AV	PX429-050AV
100	6.9	PX409-100AV	PX419-100AV	PX429-100AV
150	10.3	PX409-150AV	PX419-150AV	PX429-150AV
250	17.2	PX409-250AV	PX419-250AV	PX429-250AV
500	34.5	PX409-500AV	PX419-500AV	PX429-500AV
750	51.7	PX409-750AV	PX419-750AV	PX429-750AV
1000	69	PX409-1.0KAV	PX419-1.0KAV	PX429-1.0KAV

**Ordering Examples:** PX409-1.0KGV, mV output, 1000 psi gage pressure range, 2 m (6') cable termination. PX429-015AV, mV output, 15 psi absolute pressure, twist lock termination, PT06F10-6S, mating twist lock connector (sold separately), and DP25B-S, 4-digit meter, system with meter.  
(See page B-25h for information on meters).

**mV/V Specifications**

**Output:** mV/V, 100 mV @ 10 Vdc (Ratiometric 5 to 10 Vdc)

**Supply Voltage:** 10 Vdc (5 mA @ 10 Vdc)

**Input/Output Resistance:** 5000 Ω ±20% typical

**Accuracy (Combined Linearity, Hysteresis and Repeatability):** ±0.08% BSL maximum

**Zero Balance:** ±0.5% FS typical 1% max (1% typical, 2% maximum for 2.5 psi and below)

**Span Setting:** ±0.5% FS typical 1% maximum (1% typical, 2% maximum for 2.5 psi and below) Calibrated in vertical direction with fitting down

**Operating Temperature Range:** -45 to 121°C (-49 to 250°F)

**Compensated Temperature:**

- Ranges >5 psi: -29 to 85°C (-20 to 185°F)
- Ranges ≤5 psi: -17 to 85°C (0 to 185°F)

**Thermal Effects Zero (Over Compensated Range):**

- Ranges >5 psi: ±0.5% span
- Ranges ≤5 psi: ±1.0% span

**Thermal Effects Span (Over Compensated Range):**

- Ranges >5 psi: ±0.5% span
- Ranges ≤5 psi: ±1.0% span

Figure 0.1: Pressure Transducer Specifications

**iMAG 4700 Series**  
**FLANGED MAGMETER**

**Specifications**

<b>Pipe Sizes</b>	3", 4", 6", 8", 10", 12"				
<b>Flanges</b>	150 lb. ANSI Pattern				
<b>Pressure</b>	150 psi (10.3 bar) line pressure				
<b>Temperature Operating</b>	10° to 140° F (-12° to 60° C)				
<b>Storage</b>	-40° to 158° F (-40° to 70° C)				
<b>Accuracy</b>	±0.75% of reading on iMAG 4700p and 4700r (±1.0% iMAG 4700), ±0.025% of full-scale flow from low flow cutoff to maxi. flow rate of 10 m/sec				
<b>Low Flow Cutoff</b>	0.5% of maximum flow rate				
<b>Material</b>	<b>Body (3" only)</b>	Ductile cast iron, powder coated			
	<b>Body (4"-12")</b>	Welded steel, epoxy-coated			
	<b>Liner (3" only)</b>	Noryl®			
	<b>Liner (4"-12")</b>	Santoprene flange/Polypropylene liner body			
	<b>Electronics Housing</b>	Powder-coated diecast aluminum			
	<b>Electrodes</b>	316 stainless steel			
<b>Display</b>	<b>O-ring (3" only)</b>	EPDM			
	<b>Type</b>	128x64 dot-matrix LCD			
	<b>Digits</b>	5 Digit Rate	8 Digit Total		
	<b>Units</b>	Rate Volume Units	Rate Time Units	Total Volume Units	
	<i>Please Note: All iMAG meters are factory set for gallons per minute (GPM) rate and gallons total. If other units are required, they can be set in the field.</i>	Gallons Liters Barrels(42 gal) Cubic Feet Cubic Meters	Million Gallons <sup>2</sup> Mega Liters <sup>3</sup> Imperial Gallons Million Imperial Gallons <sup>4</sup>	Second Minute Hour Day	Gallons Gallons x 10 Gallons x 100 Gallons x 1000 Million Gallons Liters Kilo Liters Mega Liters
				Barrels (42 gal) Cubic Meters Cubic Meters x 1000 Cubic Feet Cubic Feet x 1000 Second Foot Day Million Cubic Feet	
<b>Bidirectional<sup>1</sup></b>	Forward Total, Reverse Total, Net Total, Batch Forward Total, Batch Reverse Total (Batch totals can be reset)				
<b>Power</b>	<b>DC Power</b>	9-36 Vdc @ 250 mA max, 30 mA average			
	<b>Battery Backup</b> <i>(Not for use as primary power)</i>	DC powered units: Two lithium 3.6V 'D' batteries, replaceable. AC powered units: One 9V alkaline battery, replaceable.			
	<b>AC Power</b> <i>(iMAG 4700r and 4700p only)</i>	85-264Vac, 50/60Hz, 0.12A			
	<b>Battery</b> <i>(iMAG 4700 only)</i>	One lithium 7.2V 'D' size battery pack, replaceable.			
<b>Scaled Pulse Output</b>	<b>Signal</b>	Current sinking pulse, isolated, 36 Vdc at 10 mA max			
	<b>Pulse Rates</b>	User-scalable from 0.1 to 99,999.9 volume units/pulse. Pulse width is one-half of pulse period with minimum pulse width of 2.5 ms, 200 pulses/sec max. For battery option meters, pulse width varies with frequency, 150 pulses/sec max.			
<b>Options</b>	<b>4-20mA Current Loop</b>	Isolated, passive, 24Vdc, 650 Ω maximum current loop			
	<b>HART/4-20mA</b>	HART protocol over 4-20mA line			
	<b>High Speed Digital Output</b> <i>(iMAG 4700 &amp; 4700p only)</i>	Isolated, open collector, 24 Vdc			
	<b>Serial Communications</b>	Isolated, asynchronous serial RS485 (Reconfigurable for RS232 or 3.3V CMOS), Modbus® RTU protocol (factory selectable)			
<b>Cable</b>	<b>Power/Output Cable</b>	20ft (6m) standard length polyurethane jacketed cable—for power and outputs (lengths up to 200' available).			

Figure 0.2: Magnetic Flowmeter Specifications